Einstein Telescope beampipe requirements

ET-0385A-24

Aniello Grado, Marije Barel, Tomasz Bulik, Marc Andres-Carcasona, Giacomo Ciani, Livia Conti, Julien Gargiulo, Stefan Hanke, Harald Lueck, Mario Martinez, Andrea Moscatello, Nick van Remortel, Carlo Scarcia, Emanuele Tofani, Patrik Werneke

Issue: 1

Date: July 2, 2024

ET – Einstein gravitational wave Telescope – Design Study * A joint European Project
Web: http://www.et-gw.eu Email: EuropeanProjectsService@ego-gw.it

Contents

1 Introduction

This document aims to establish the scientific requirements of the Einstein Telescope (ET) beampipe vacuum system. Scientific requirements encompass all requisites concerning the beampipe vacuum system that may impact the ultimate sensitivity of the detector. Many specific engineering requirements of the beampipe (just to mention a few examples: types of welds, types of pumps, etc.) are the subject of studies by CERN and do not fall within the scope of the present document, but will be part of the TDR that has been commissioned to CERN. The definition of beampipe system requirements falls under the ISB responsibility.

The document's composition has undergone a more detailed process than initially anticipated. This decision was made to formulate requirements as closely aligned with engineering specifications as possible, thereby facilitating their practical implementation. While the primary parameters have been established, the document remains incomplete, as certain requirement values necessitate more in-depth studies and additional simulations that are not presently available. Consequently, the document should be regarded as a dynamic resource subject to periodic updates.

In table 1 we report the still open issues that will be the subject of further studies.

Issue #	short description
1	Optimization of baffles (including position, optical quality, vibration and number of baffles
2	Noise induced by large mirror phase map
3	Review requirements on baffles vibration
4	Transmission of vibrations through the floor or ground, from the tunnel to the experimental hall, when there is a large mass such as pipes vibrating at low frequencies.
5	Optimization of the baffles apertures taking into account the effect of the induced stray-light noise
6	in figure 16 the effective baffles displacement can not be 10 m/sqrt(Hz)
7	to be added to section 8 a subsection on leak detection for beampipe quality assessment
8	to be added to section 8 a subsection on sectorization
10	make new scattering calculation assuming updated dimensions in the cryo area
11	make new scattering calculation to evaluate the effect on noise due to reduced inner size baffles
12	make different scattering calculations to evaluate noise with different assumed distances between towers and cryotraps
13	extend all the calculations to L shape 15 km arms length

Table 1: Beampipe requirements open issues.

For clarity, Table 2 lists all the key parameters related to the beampipe vacuum system.

Symbol	Value ET-LF	Value ET-HF	Units	Description
R	0.5	0.5	m	Beampipe radius
D_{tunnel}	6.5	6.5	m	Tunnel diameter
L	10	10	km	ET arms length
λ	1064	1550	nm	Laser wavelength

Table 2: Beampipe vacuum system general parameters.

1.1 What encompasses the beam pipe vacuum system? (M.Y. Barel, J. Gargiulo, A. Grado)

The requirements need to encompass details for both configurations of the Einstein Telescope: the triangle configuration and the 2L-configuration. In this document version (april 2024) more parameters are known for the triangle configuration, as such all the current requirements apply to that configuration.

To read about the basic concept design of the triangle configuration read: "Design report update 2020, for the Einstein Telescope." [14]. Figure 1 shows the general idea of the beam pipe vacuum system concept based on the triangle configuration. However, we only see one high-frequency and one low-frequency beam pipe, which is indicative to a L-configuration.

The requirements in this document intent to drive the design solution, not the other way around. In practice however this a dynamic process.

We consider the beam pipe vacuum to be:

- The beampipe encompasses the pipes linking the Input and End Test Masses, excluding the cryogenic sections, but including the large valves, support structure, bakeout apparatus, pumping system and vacuum measurement instrumentation. Other pipes are not in the scope and fall within the 'Tower Vacuum' or related sections
- The beam pipe vacuum system influences partially other systems, these are referred to in the interfacing section of this document

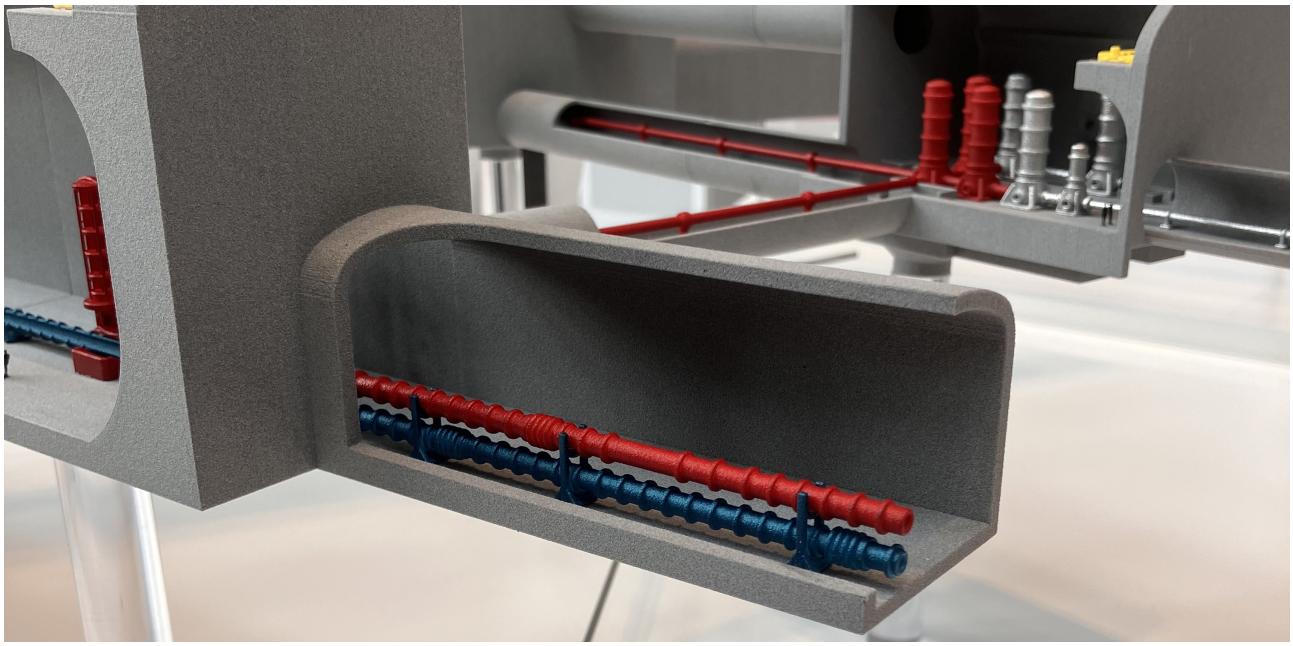

Figure 1: 3D printed concept of the Einstein Telescope created by Marco Kraan located at Nikhef

- It is presumed that the vacuum within the beam pipe and that within the towers are entirely independent due to the implementation of cryotraps.
- We cannot assume the number of pipes, nor there location in the tunnel.
- We do not consider baffles near the main mirros. They are very relevant but at the moment are out of scope.

2 Scattering light (M. Martinez, Marc Andres)

In the following, we present an estimation of the noise induced by scattered light inside the main arms of ET. Both ET configurations for high- and low-frequency interferometers are considered, for which we propose baffle layouts. The noise estimations are computed using analytical calculations complemented with numerical tools, and depend on several baseline parameters we use as input in the calculations. The level of scattered light and the ET laser beam clipping losses are intimately related to the baffle's inner aperture. We discuss how this translates into minimum requirements on the vacuum pipe radius, a critical parameter in the ET design.

We use default parameters for the ET-LF and ET-HF optical configurations in the triangular baseline design, as collected in Table 3[1]. The work is focused on the baffle configuration in the bulk of the vacuum sections in the main arms. In the future, work will be extended to cover the areas close to the test masses at distances of about tens of meters, which require a separate study.

2.1 Beampipe diameter

The proper definition of the vacuum pipe hosting the laser beam in the main arms constitutes a major milestone in the design of the whole experiment, since it introduces strong constraints over the rest of the detector elements and, to a large extent, conditions the total cost of the project. One of the most important aspects to take into

[1]Here we consider a cartesian right-handed coordinate system with origin in the input mirror of the optical cavity and the z-axis along the laser beam line. The azimuthal angle φ is measured around the beam axis and the polar angle θ is measured with respect to the z-axis.

FP optical cavity parameters				
Variable	ET-HF	ET-LF	Units	Description
m	200	211	kg	Mirror mass
L	10	10	km	Length of an arm
λ	1064	1550	nm	Wavelength of the laser
R_m	0.31	0.225	m	Radii of the mirrors
$\mathcal{R}_1$	5070	5580	m	Radius of curvature input mirror
$\mathcal{R}_2$	5070	5580	m	Radius of curvature end mirror
P_{circ}	3000	18	kW	Circulating power in the cavity
R	0.5	0.5	m	Radius of the vacuum pipe.

Table 3: Parameters of the ET main FP arm cavities. The values are extracted from Refs. [13, 14].

account in establishing the parameters of the vacuum pipe is the control of stray light propagating in the optical cavities, which, if not properly addressed, has the potential to limit the interferometer sensitivity as a whole.

In particular, the size of the beampipe is conditioned by the optical aperture required to maintain at negligible levels the clipping losses inside the cavity. In the ET Fabry-Perot (FP) optical cavities, the laser beam has a Gaussian-shaped transverse profile, with maximum beam sizes close to the mirrors at both ends of the FP cavity. In a configuration with the laser beam centered inside the beampipe, the power decreases with increasing distance to the tube longitudinal axis following the Gaussian profile [2], and the beam losses are dictated by the limited apertures inside the vacuum tube.

We define the clipping losses as $L_c(r,z) = 1 - P(r,z)/P_0$, where $P(r,z)$ is the power in cavity in a given position and P_0 denotes the total power in the cavity. The required beampipe radius in a given z position and at a given level of losses L_c can be expressed in terms of the beam size $w(z)$ (defined as the radius at which the field amplitude decays by a factor $1/e$) [3] as

$$r(z, L_c) = \frac{w(z)}{\sqrt{2}} \sqrt{\ln\left(\frac{1}{L_c}\right)} + r_{\text{offset}}, \tag{1}$$

where r_{offset} is an additional term to include eventual offsets of the beam with respect to the cavity longitudinal axis. Following the expressions above, Fig. 2 presents iso-losses curves as a function of the z-position in the optical cavity for both ET-HF and ET-LF interferometers, with $r_{\text{offset}} = 0$.

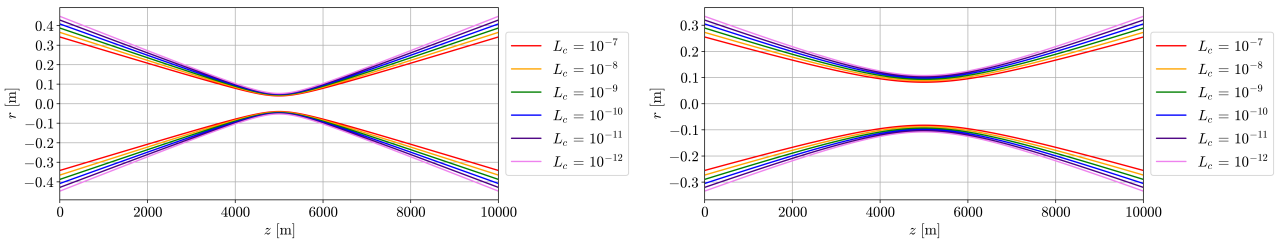

Figure 2: Beam profile as a function of the position in the arm z at different levels of clipping losses L_c for (left) ET-HF and (right) ET-LF interferometers (taken from Ref. [3]).

We adopt the criteria that the clipping losses will be maintained at the level $L_c < 10^{-8}$. This clipping losses threshold is set following the previous works by LIGO and Virgo as a starting value to iterate the design, since the ultimate requirement for the aperture is dictated by the resulting scattered light noise. The value $L_c < 10^{-8}$ is regarded as a conservative number to ensure that the inner apertures of the baffles do not clip the field more

[2] It is important to mention that the simplification of using a Gaussian profile is limited to the calculation of the clipping losses as a first step in determining an initial value for the apertures. The calculations of the scattering noise are based on a full simulation of the beam profile, including higher-order modes and mirror maps.

than the actual mirrors [3]. Evaluating $r(z = 0, L_c = 10^{-8})$ yields $r_{\mathrm{ET-HF}} \simeq 0.42$ m and $r_{\mathrm{ET-LF}} \simeq 0.31$ m, after including a beam offset of $r_{\mathrm{offset}} = 5$ cm. We assume that larger offsets, such as those caused by ground subsidence, can be compensated for by using specifically designed tube support mechanisms. These numbers represent the minimum possible inner apertures for the ET-HF and ET-LF interferometers. In ET, baffles are installed inside the vacuum pipe to prevent noise due to scattered light from the mirrors reaching the inner walls of the vacuum pipe and re-coupling to the interferometer main laser mode. Therefore, the figures above also represent the minimum baffle inner apertures. For a typical baffle vertical height in the range of 8 cm to 10 cm the required aperture translates into a minimum beam pipe radius of $R_{\mathrm{ET-HF}} \simeq 0.5$ m and $R_{\mathrm{ET-LF}} \simeq 0.4$ m.

2.2 Decision on beampipe diameter taken at the XII ET Symposium (A. Grado)

During the ET Symposium held in Cagliari from 8 to 12 May 2023, one of the focal points of discussion revolved around the beampipe diameter. The determination of this value holds significant importance as it directly impacts the sizing of the tunnel and serves as a crucial input for the CERN group in achieving a Technical Design Report (TDR) for the beampipe vacuum system.

Essentially, the beampipe diameter is contingent upon the clipping factor, which is closely associated with the geometric properties of the laser beam, as well as the allowance required for potential future upgrades of the ET detector. The initial calculation, as described in the previous section, assumes a clipping loss of 10^{-8} and mirror sizes of 62 cm and 45 cm for ET-HF and ET-LF respectively. Consequently, this yields clear apertures of 84 cm and 62 cm for ET-HF and ET-LF respectively. Additionally, the size of the baffle, contributing an additional 16 cm, is factored in, resulting in overall dimensions of 100 cm and 78 cm.

However, projecting the beampipe diameter for future ET upgrades proves to be a more intricate task. Extensive discussion during the hot topic wrap-up session of the ISB on May 10th, specifically addressed this aspect. It was concluded that an increase in mirror size for ET-HF is unlikely, whereas it could occur for the low-frequency counterpart, ultimately leading to an identical mirror size for both low and high-frequency detectors. Subsequently, after thorough discussion, a general consensus was reached to adopt a **beampipe diameter of 100 cm for both detectors**.

2.3 Projected scattered light noise

The currently operating LIGO and Virgo ground-based experiments implemented a set of conical baffles inside the main interferometer arms, with the purpose of mitigating the scattered light noise by geometrically shielding the beampipe (and any internal structure on its surface) from photons scattered by the main mirrors in the FP cavities. A simplified scheme of the geometry is displayed in Fig. 3. Table 4 collects relevant baffle parameters.

The distance W in Fig. 3 represents the farthest point from which a photon should be shielded. We follow the conservative approach in Ref. [19] and adopt the maximum possible value corresponding to the sum of the beam pipe radius (R) plus half of the radius of the mirror (R_m), $W = R + R_m/2$. The distances a_i are taken from ET design reports in Refs. [4, 14] and correspond to [4]:

- a_1: Distance between the mirror and the beginning of the main arm beampipe [2.35 m].
- a_2: Distance between the end of the tower and the beginning of the cryopump area [20 m]
- a_3: Length of the cryopump area [10 m for ET-HF and 50 m for ET-LF].
- a_4: Distance between the end of the cryopump area and the first baffle in the main arm. In this work it will be set to 0 m, meaning that the first baffle is assumed to be placed just after the cryotrap.

With the values for W and a_i above, we establish the position of the first baffle. These positions are $z_0 = 32.35$ m and $z_0 = 72.35$ m for ET-HF and ET-LF, respectively. It is important to note this work is limited to describing

[3] Work is in progress to illustrate the effect of a $L_c < 10^{-6}$ threshold (with reduced apertures) on the computed scattering noise.

[4] Recent (april 2024) interactions with experts designing the cryopump areas point to the following revisited values: $a_1 = 2$ m, $a_2 = 0$ m, $a_3 = 10$ m also for ET-LF. Although we expect no significant effect in the main results for the induced scattering noise, those updated a_i values are now being used for the next iteration of the analysis.

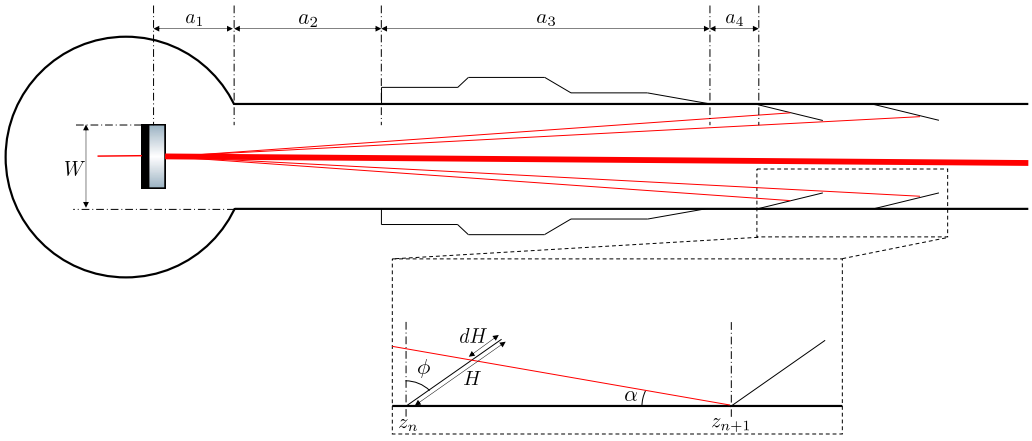

Figure 3: Simplified diagram showing the area of the ET main arm close to the mirror and the geometry and parameters determining the position and shape of the conical baffles (taken from Ref. [3]).

the baffle layout in the bulk of the interferometer's main arms. No attempt is made to discuss the stray light mitigation strategy close to the mirrors and inside the cryotrap areas, which constitutes the subject of future studies.

The main source of scattered light noise that we consider here is the one generated by the light scattered by the mirrors. This includes two contributions: the mirror's finite aperture and its surface aberration. Any deviation from the perfect surface causes photons to follow a different path than that intended. To study this effect and characterize the mirror surface defects, mirror maps or phasemaps are used. A measure of the surface map quality is the spatial power spectral density (PSD), related to the two-dimensional Fourier transform of the function $\delta(x, y)$ describing the height of the mirror surface at a given $x - y$ location. Here, a one-dimensional PSD is used [3], which takes into account that the surface structure is not necessarily cylindrically symmetric and integrates over the azimuthal angle in the $x - y$ plane. Based on such mirror maps [5], a detailed estimation of the scattered light noise has been performed [3], where four different noise sources are initially considered:

- *Diffraction.* The limited inner apertures of the baffles produce a diffraction pattern that can limit the sensitivity of the interferometer. This noise contribution depends on the number of baffles placed inside the beampipe and their geometry, as the single noise contributions from each baffle can pile up coherently. The main mitigation strategy is to break this coherence, which can be achieved by serrating the edges of the baffles as has been done in the case of LIGO and Virgo [6, 48, 17, 19, 18, 51]. This reduces by about two orders of magnitude its contribution to the scattered light noise budget. Additionally, extra radiation pressure to the test masses can be relevant at low frequencies.

- *Backscattering.* This is caused by photons that after being scattered by one of the mirrors reach another surface, such as a baffle, where they scatter again and reach any of the mirrors. These photons can recombine with the main beam and, bringing a different phase, limit the sensitivity of the interferometer. Again, extra radiation pressure to the test masses becomes relevant at low frequencies. Here, we mainly consider the effect of backscattering and not the reflection as due to the angle of inclination of the baffles it has been estimated to be subdominant. The vast majority of photons being reflected will bounce many times off the tube and other baffles, probably being re-absorbed before reaching any of the mirrors. In the case of the noise estimation, the side looking at the far end mirror is considered, as more light is going to reach from it compared to the closer mirror.

- *Baffle edges.* Baffles are inclined exposing to photons their edges. In principle, photons can be reflected on these edges and reach any of the mirrors. A simple solution to virtually eliminate this noise contribution is also that of serrating the baffle edges.

[5] In the case of large optics, there is uncertainty to how the mirror map might look like, as there are effects of the polishing and coating machines that should be considered. The production of refined mirror maps is work in progress.

- *Shinning facet.* In principle, any piece of reflective material inside the beampipe can be a source of significant scattered light noise as any strayed photon can be directly reflected back to any of the mirrors. Such reflective surfaces can be produced during the machining of the tube or by equipment placed inside it. This effect is totally suppressed by placing baffles such that no strayed photon can reach the bare structure of the beampipe.

Baffle parameters				
Variable	ET-HF	ET-LF	Units	Description
A_b	0.84	0.84	m	Baffle inner aperture ($R = 0.5$ m)
H	0.14	0.14	m	Baffle length
dH	0.0244	0.0244	m	Baffle overlapping factor
ϕ	55	55	deg	Inclination angle of the baffles
$\frac{dP}{d\Omega_{bs}}$	10^{-4}	10^{-4}	str^{-1}	BRDF of the baffles

Table 4: Parameters of the baffles inside the ET vacuum.

Following the considerations above, only the backscattered and diffraction noise contributions are further analyzed. The rest of the noise sources are orders of magnitude smaller, provided the recommendations related to the baffle layout inside the beampipe and the serration (see details in [3] and Section 9.5) of the baffle edges are followed.

In the case of the diffraction noise contributions, the results are computed adopting Eq.(23) in Ref. [3] and the seismic noise levels from the Euregio site. The same calculation can be done if the Sardegna seismic noise curve is used.

For illustration purposes, the results are presented in Fig. 4 for both smooth (unserrated) and randomly serrated baffle edges, separately for ET-HF and ET-LF. As already pointed out, the serration of the baffle edges is mandatory and its implementation brings the diffraction noise to acceptable levels.

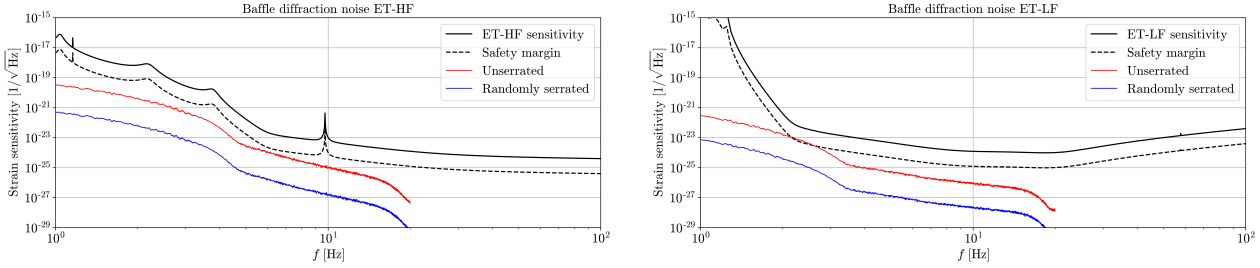

Figure 4: Stray light noise due to diffraction effects as a function of frequency. The results for unserrated (red lines) and randomly serrated (blue lines) baffle edges are compared to the anticipated ET sensitivity (black lines) and the corresponding 1/10 safety margin (dashed lines). The results are presented separately for (left) ET-HF and (right) ET-LF configurations. The seismic noise data from the Euregio site are used.

Figure 5 shows the resulting backscattering noise separately for ET-HF and ET-LF configurations. In both cases, the predicted noise curve is more than one order of magnitude below the expected ET sensitivity [46], indicating that the scattered light noise in the main cavities, dressed with baffles, should not be a limiting factor for the sensitivity of the experiment.

In Ref. [3], the scattering noise is recomputed for a modified ET-HF configuration with a larger beampipe radius (1.2 m) and larger baffle apertures (1.04 m). As expected, the larger aperture results in a large reduction in the scattered light arriving at the baffles. It turns into a further 50% reduction in the predicted backscattering noise. The total noise is reduced by about 35%, dominated by the diffraction noise contribution. Finally, the study considers the scenario of a possible ET-LF upgrade with larger mirrors with a slightly different radius of curvature. Although this translates into an about factor two increase in the backscattering noise, the

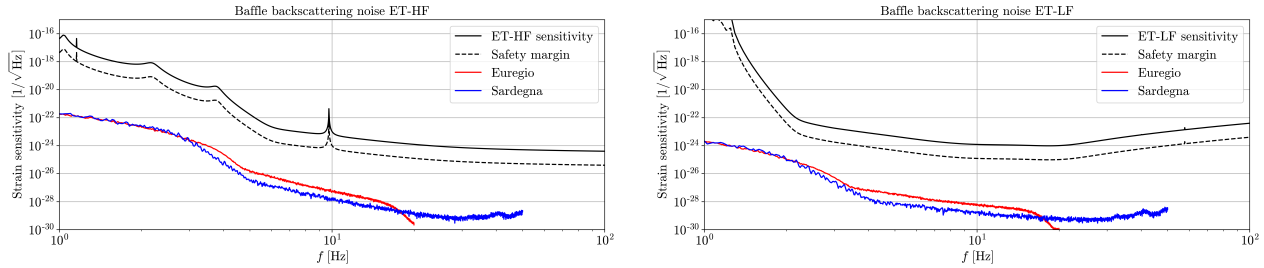

Figure 5: Stray light noise due to backscattering effects as a function of frequency. The results are computed using the seismic noise data from the Euregio (red lines) and the Sardegna (blue lines) sites and are compared to the anticipated ET sensitivity (black lines) and the corresponding 1/10 safety margin (dashed lines). The results are presented separately for (left) ET-HF and ET-LF (right) configurations.

total scattering noise is dominated by the diffraction contribution that remains unchanged and well below the anticipated ET-LF sensitivity. As mentioned above, work is in progress to illustrate, for completeness, the effect of reduced apertures on the total noise.

The numerical simulation above does not include the effect of disturbances in the field inside the cavity due to the presence of the baffles themselves. However, this effect is small and is not expected to change the conclusions. Further studies are in preparation, incorporating the baffles in the simulated geometry. This will translate into a refined estimation of the noise, particularly relevant for the case of diffraction contributions which are now computed analytically. This development will also facilitate the study of the noise in non-ideal configurations and with significant laser beam miss-alignments. The latter might translate into new requirements on the lateral positions of the baffles, linked to the overlapping requirements of the baffle projections as viewed from the mirror.

Similarly, the upper bounds on stray light noise can be translated into upper limits on the level of vibrations of the infrastructure which remain acceptable, once the spectra of vibrations are provided in time and frequency domains and the transfer functions relating the vibrations of the ground, the beam pipe and the installed baffles are known. This information is not available at this time. In Sec. 9.4 we provide upper bounds on the acceptable level of vibration of the baffles themselves, as extracted directly from the results above.

Scattering light requirements				
Requ. number	Name	Value	Units	Description
Req.1	*D-HF*	1	m	Beampipe diameter for HF
Req.2	*D-LF*	1	m	Beampipe diameter for LF, it takes into account future upgrade
Req.3	*BiD-HF*	0.84	m	Baffle inner diameter for HF
Req.4	*BiD-LF*	0.84	m	Baffle inner diameter for LF
Req.5	*Bϕ-HF*	55	deg	Baffle inclination angle for HF
Req.6	*Bϕ-LF*	55	deg	Baffle inclination angle for LF
Req.7	*BBRDF-HF*	10^{-4}	deg	Baffle BRDF for HF
Req.8	*BBRDF-LF*	10^{-4}	deg	Baffle BRDF for LF
Req.9	*DLA-HF*	0.022	m	Maximum lateral deviation from nominal position for two consecutive baffles for HF
Req.10	*DLA-LF*	0.022	m	Maximum lateral deviation from nominal position for two consecutive baffles for LF
Req.11	*DLA-HF*	0.05	m	Maximum offset between laser axis and beampipe axis for HF
Req.12	*DLA-LF*	0.05	m	Maximum offset between laser axis and beampipe axis for LF
Req.13	*NB-HF*	118	#	Minimum number of baffles for HF (PRELIMINARY VALUE)
Req.14	*NB-LF*	90	#	Minimum number of baffles for LF (PRELIMINARY VALUE)
Req.15	*TPB-HF*	0.02	m	Tolerance in the longitudinal baffle position for HF
Req.16	*TPB-LF*	0.02	m	Tolerance in the longitudinal baffle position for LF

Table 5: Requirements derived from scattered light studies

3 Scattering by particles. (L. Conti, G. Ciani, A. Moscatello)

Particles, eg of dust, present inside the ET vacuum pipes can be a concern as they can be a source of scattered light. It is therefore important to quantify the noise light-dust interaction can originate so as to be able to put constraints on the maximum allowed population of particles in the vacuum pipes. It is also important to understand how the distribution of particles that may interact with light evolves in time as well as identify the events that may introduce particles inside the vacuum pipes, to minimize contamination.

The scattering of light by particles is fully described by the Mie theory. Typically we are mainly concerned by particles of the size about 0.1-100μm: smaller particles, even if more numerous, are expected to contribute less to the scattering. However, the theory we use is applicable in a wider range of dimensions.

We do not consider here the problem due to particles present in the towers housing the Test Masses (TM) or on the TM themselves, but we are only concerned with the particles in the pipes. We can identify two main occasions for light-particles interaction:

- when a particle deposited on a pipe surface, typically a pipe baffle, is hit by light coming from the main beam
- when a particle crosses the beam, eg if falling from the pipe internal top surface

In addition we consider only light coming directly (ie without any additional interaction) from a Test Mass, reaching a particle and from there reaching a TM again directly without any further interaction. Here, it needs to be rescattered into the main beam. In other words, we do not consider multiple scattering by particles nor further scattering or reflection events by baffles or pipe tube. Overall we are considering the same scattering order as light backscattered by the clean baffles and originating the baffle backscattering noise.

The two cases listed above require quite different approaches: in the first case we need to estimate the worsening of the scattering properties of the baffles due to the dust deposited on their surfaces, that is the additional BRDF contributed by the deposited particles. In the second case we need to quantify the phase noise added by the

light reaching the TM after being scattered by a random population of particles crossing the main beam. In the following, we discuss separately the two contributions, respectively in sec.3.1 and sec.3.3. More specifically, in sec.3.1:

1. we describe how dust deposited on baffles can contribute to light scattering; see fig.6 and eq.(2)
2. we study the effect of particles that deposit on baffles while they are still in air. We distinguish two cases: (a) dust deposited while the baffles are handled in a cleanroom, and (b) during the storage of pipe sections where baffles have been installed till the end of the pipe production. For such cases:
   (a) From the particle distribution eq.(4) and fig.9, using eq.(2) we size the scattering due to dust, which we compare with that due to the clean baffles. Then we conclude with a recommendation for the clean room class when assembling the baffle in the ET pipes section, as a function of the exposure time of parts in air.
   (b) we discuss the impact of the pipe full assembly wrt to cleanliness and give some recommendations for the storage of the parts of the beam pipe once they are ready.
3. we estimate (c) the amount of dust particles that can deposit on baffles while they are already under vacuum. We compare this with the particles that might have deposited earlier, when in air, and conclude about the relevance of the contamination added while in vacuum

3.1 Dust deposited on baffles

We consider here the effect in terms of scattering of the dust that deposits on the baffles: the net effect is to worsen the baffle's performance in terms of bidirectional reflectance distribution function (BRDF, indicated as $dP/d\Omega_{bs}$ in table 4). This enters as a square root in the baffle backscattering contribution to the strain noise [31] [52], as shown in sec.2.3.

Because of the deposited dust, under the assumption of low scattering levels, the total BRDF that needs to be used for computing the baffle backscattering noise is the sum of the contributions from baffle and dust: BRDF = BRDF_{baffle}+BRDF_{dust}. The latter depends on the dust dimension and material as well as on the numerosity: this last term brings in a time dependence as dust particles continue to accumulate both when the baffles are in air and also when in vacuum, as explained later in this section.

The BRDF_{dust} for a distribution of particles deposited on a surface, described by the particles density $f(D)$ (representing the number of particles with diameter D per unit area) is [44] [16] :

$$\mathrm{BRDF}_{dust}(\lambda, m, \theta_s, \theta_i) = \frac{1}{k^2 \cos(\theta_s)} \times \sum_D f(D) \left[\frac{2R_f(|S_1(x,m,\theta_f)|^2 + |S_2(x,m,\theta_f)|^2) + |S_1(x,m,\theta_b)|^2 + |S_2(x,m,\theta_b)|^2}{2} \right] \quad (2)$$

where $x = \pi D/\lambda$ is the size parameter of the particles, assumed to be spherical, λ is the laser light wavelength, $k = 2\pi/\lambda$, R_f is the baffle's reflectivity (which is assumed to be constant at all angles), and θ_i and θ_s are the angles of the incident and scattered light with respect to the normal to the surface in the plane of reflection. Light backscattered at $\theta_s = -\theta_i$ arrive directly to the Test Masses (see Figure 6): thus we are concerned with $\mathrm{BRDF}_{\mathrm{dust}}(\theta_i = 55°, \theta_s = -55°)$: this is to be compared and summed with the values of BRDF expected for the baffles. Here the indices b and f refer respectively to the rays that are scattered in the backward and forward direction: in particular the rays scattered in the forward direction are those reaching the baffle surface under the dust particle, where they are specularly reflected. We are interested in the scattered rays that propagate back to the same TM where they originated from. Given our particular geometry (baffle inclined at 55° and light incident on the baffle at $\theta_i \sim 55°$ - Figure 6), there are three cases for this to happen (computing the angles of the scattered rays with respect to the direction of the incoming light):

1. rays scattered at an angle $\theta_b = \pi$ (i.e. light 'back' scattered at $\theta_s = \pi - \theta_b - \theta_i$)

2. rays scattered at an angle $\theta_f = \theta_s - \theta_i$ (i.e. light 'forward' scattered at $\theta_s = \theta_f + \theta_i$: it reflects off the baffle before returning towards the TM).
3. light arriving at the baffle at an angle $\theta_i = 55°$ with respect to the baffle's normal, being specoularly reflected onto the particle and being scattered to the TM at an angle $\theta_f = \theta_s - \theta_i$.

The third contribution is analogous to the "forward-scattered" contribution represented in fig.6 but with reversed arrows. Given our specific geometry, those two contributions are formally the same as the scattering in both cases is computed as $\propto R_f(|S_1(x, m, \theta_f)|^2 + |S_2(x, m, \theta_f)|^2)$. This is the origin of the factor 2 in front of the forward contributions in eq.2.

The complex quantities $S_{1,2}$ are the Mie scattering matrix coefficients (estimated with the python package "MiePython" [39]), where the indexes $1, 2$ refers to the polarization perpendicular and parallel to the scattering plane respectively. In our study, we have worked with unpolarized light. The quantity m is the complex index of refraction of the dust material. Experimental investigations on refractive indexes of environmental dust indicate that the real and complex parts vary respectively in the range (1.3 , 1.8) and (10^{-4}, 0.8) for light wavelengths between 1 and 2 μm [24] [42].

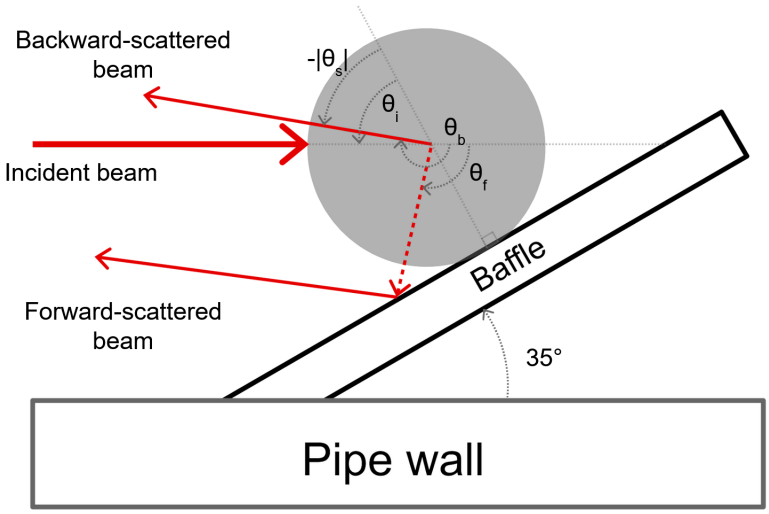

Figure 6: Geometry for Mie scattering from a spherical particle deposited on a baffle inclined at 55°. The incident and scattered angles, θ_i and θ_s, are the directions of the incident and scattered rays with respect to the normal to the baffle surface, respectively anticlockwise and clockwise. The picture also shows the angles θ_f and θ_b of the forward and backward scattered rays. For the geometry of ET $\theta_i \sim 55°$, we consider the light scattered at $\theta_s = -\theta_i$ (going back to the TM). We note that the model of eq.(2) assumes that the radiation scattered in the forward direction reflects from the mirror and does not interact again with the particle.

To set cleanliness requirements for ET, using eq.(2) we estimate the maximum number of particles we can tolerate on each baffle before the dust-contributed BRDF (called $BRDF_{dust}$) equals the BRDF of the clean baffle at $\theta_s = -\theta_i = -55deg$ (called $BRDF_{baffle}$). We take as reference $BRDF_{baffle} = 1 \times 10^{-4} sr^{-1}$, as shown in Table 4. Because of the dependence on the particle size expressed by the variable x in eq.(2), the maximum tolerable number of particles depends on their size. Thus we are led to set a requirement on the maximum number of particles per a given size range that we can tolerate on each baffle in order for $\int_{0.1\mu m}^{100\mu m} BRDF_{dust}(x)\, dx \leq BRDF_{baffle}$ at $\theta_s = -\theta_i = -55deg$: we assume the particles to be distributed homogeneously on the baffle surface and to have a flat distribution in each size bin. In addition, we need to explore the range of values that the dust particle's refraction index m can assume. In our estimates, we assume that all particles have the same complex value of m, that this may vary in the range $(1.3 - 1.8) + i(10^{-4}, 0.8)$ with uniform probability, and compute the $BRDF_{dust}$ corresponding to the 50% and 90% percentiles. Table 6 shows the result of these computations: this is the cleanliness requirement that we set for the ET baffles. We note that we have no hint at this stage of what the most probable refraction indexes are for dust in ET;

	Density (particles/m^2)		
diameter range (μm)	50%	90%	$m = 1.5 + i\,10^{-3}$
(0.1 - 0.3)	$9.3 \cdot 10^{11}$	$6.2 \cdot 10^{11}$	$2.0 \cdot 10^{12}$
(0.3 - 1)	$1.5 \cdot 10^{11}$	$1.1 \cdot 10^{11}$	$5.7 \cdot 10^{10}$
(1 - 3)	$2.0 \cdot 10^{10}$	$1.4 \cdot 10^{10}$	$6.4 \cdot 10^{8}$
(3 - 10)	$2.1 \cdot 10^{9}$	$1.4 \cdot 10^{9}$	$1.1 \cdot 10^{8}$
(10 - 30)	$2.3 \cdot 10^{8}$	$1.5 \cdot 10^{8}$	$2.5 \cdot 10^{7}$
(30 - 100)	$2.2 \cdot 10^{7}$	$1.4 \cdot 10^{7}$	$4.5 \cdot 10^{6}$

Table 6: For each particle diameter range shown in the left column we quote the maximum number density of particles on each baffle such that $BRDF_{dust} = BRDF_{baffle}$ at $\theta_s = -\theta_i = -55deg$. Assuming that the particle index of refraction is the same for all particles and that it may vary within the interval $(1.3, 1.8) + i(10^{-4}, 0.8)$ with uniform probability, we compute the distributions that give the 50% and 90% percentiles of the maximum tolerable particle density. We also compute the maximum distribution in case the refraction index of dust assumes the value of $m = 1.5 + i\,10^{-3}$ which is most commonly found in the literature. This table constitutes the requirements for the cleanliness of the ET-HF baffles: very similar values are found for ET-LF.

furthermore, we note also that in the literature if one single value is assumed this is typically $m = 1.5 + i\,10^{-3}$ for the ET wavelengths [16].

For the particle distributions of table 6, using eq.(2), we plot in Figure 7 the resulting BRDF curves as a function of the scattering angle, for $\theta_i = 55$deg. Here we sum up the backscattering and forward scatting contributions and we assume the baffle reflectivity to be $R_f = 10^{-2}$ and for all incident and scattering angles. We show the results for ET-HF: those for ET-LF are very similar. A pronounced peak in the BRDF emerges at $\theta_s = -\theta_i$ by accounting for all the values of the complex index of refraction. We find that it is only due to particles with diameter $\geq 10\mu$m. The peak is present only when the BRDF assumes values in the extreme percentiles: such extreme values are due to extreme values of (mainly the imaginary part of) the refraction index, i.e. for $m \sim 1.8 + 10^{-4}i$. In particular, the peak is not present for the standard value $m = 1.5 + i\,10^{-3}$. Fig.7 shows also peaks symmetric with respect to $\theta_s = -\theta_i$: they are only due to the backward contribution. Possibly, they are a feature coming from the assumption of perfectly spherical particles. This will be tested experimentally.

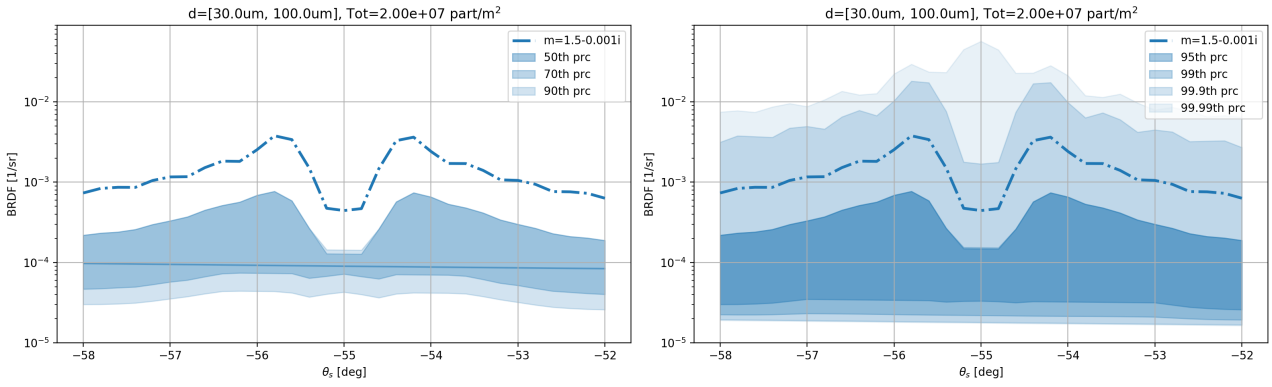

Figure 7: The BRDF contributed by particles in the range $(30 - 100)\mu$m in a small range of angles around $\theta_s = -\theta_i$. The shaded areas cover the results obtained with different values of the refraction index m which we sample uniformly in the interval $(1.3, 1.8) + i\,(10^{-4}, 0.8)$. The solid-dashed line is the prediction for $m = 1.5 + i\,10^{-3}$.

We also study the effect of the reflectivity R_f of the baffles, which enters in the contribution of the forward scattering, as shown in eq.(2). We find that for $m = 1.5 + i\,10^{-3}$, particle forward is negligible with respect to the back scattering, at $\theta_s = -\theta_i$. The relative importance of the forward scattering is higher for values of the

imaginary part of m in the upper part of the range. In such cases, the ratio forward/backward becomes $\sim R_f$. Hence for $R_f \ll 1$ the BRDF is dominated by the backward contribution and is then independent of R_f.

In the remaining part of sec.3.1, we consider a possible scenario for installation of the ET beam pipe, which we outline in paragraph (a) at page 13 and in fig.8. For this case study, we quantify the expected contamination level, which we can compare with the requirements of table 6: we study the dust that accumulates on the baffles while they are in air, distinguishing between when baffles are handled in clean room (paragraph (b) at page 13) and when pipe sections are installed and stored (paragraph (c) at page 15).

Once the contamination before vacuum is pumped is quantified, finally in paragraph (d) at page 16 we estimate the dust that may fall on the baffles while the pipes are in vacuum. This contribution is also compared with the requirements of Table 6.

(a) Pipe installation scenario The construction process of the arm pipes and the installation of the baffle is an important process from the viewpoint of cleanliness. Thus to estimate the amount of deposited dust we need first to understand the process of pipe arm building. At the moment of writing the most realistic procedure, which also minimizes the risk of dust contamination, is summarized in the following and visually represented in fig.8:

1. Tube sections are produced at manufacturer.
2. Ears are welded to those sections that need to host baffles, close to one of the ends.
3. Tube sections (with and without ears) are cleaned, sealed at both ends and shipped to the ET site.
4. A tube section is moved underground and put in place in the tunnel: one end is faced to the free end of the last installed section.
5. A clean tent is moved so that it encloses the two ends of the facing sections.
6. If a baffle is to be installed close to the junction of the new section with the existing pipe, the end of the pipe hosting the baffle (which can be either the existing one or the new one) is opened.
7. The baffle is installed to the ears using screws.
8. The seal of the other end to be welded is opened.
9. The new section is put in contact with the last installed section.
10. The tent is moved away and the two joined ends are welded together.
11. Ready for installation of next section

The whole procedure is repeated for all the sections. By following this procedure all of the instances where dust can enter occur only in a clean environment: they are described from points 6 to 9. Then while in steps 10-11, all particles entered in the pipe sections have time to deposit. In the following, we study these occurences separately.

(b) Baffles in clean room Here we consider the particles that can accumulate on the baffles while they are in the cleanroom environment, i.e. steps 6-9 in the procedure outlined at page 13. We consider that baffles are handled in clean rooms: we need to refer to realistic cleanroom classes to be realized in the underground environment. As an example, we look at the experience in particle accelerators running in UHV: "For accelerator assemblies often class ISO 4 and ISO 5 are used. In mobile cleanroom tents in accelerator tunnels local environments of class ISO 5 can be established" [30]. We thus consider class ISO 5 or worse to be realistic cases for the working environments while the ET baffles will be handled during installation.

The ISO class is defined by requirements on the volumetric distribution C_n of particles with diameter $\geq D$ allowed in the clean room, which we model following the ISO standard [20]:

$$C_n(D) = 10^{N_{ISO}} \left(\frac{0.1}{D}\right)^{2.08} \left[\frac{1}{m^3}\right] \tag{3}$$

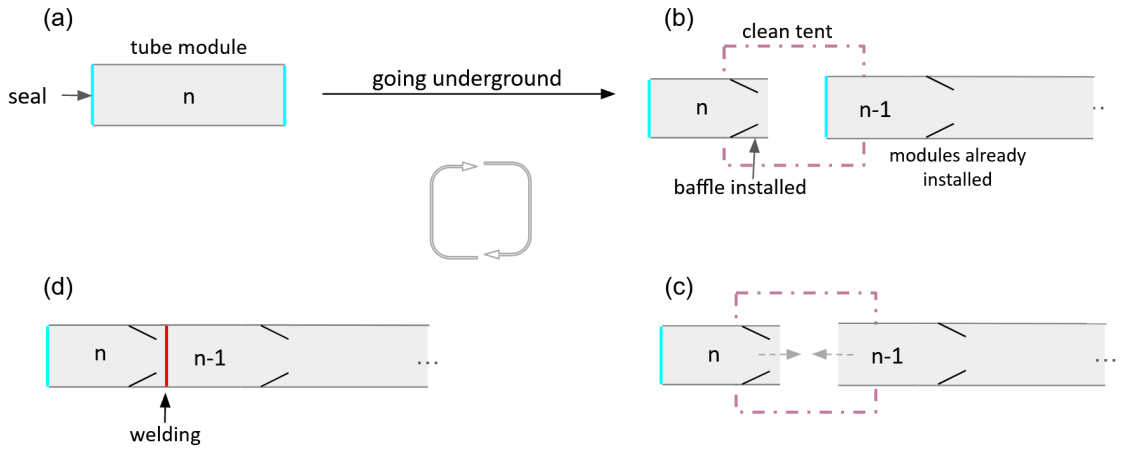

Figure 8: Visual representation of the pipe sections installation procedure, to be read clockwise: the light blue line represents the seal, the black tilted lines represent a baffle and the red line represents a welding between tube modules. The drawing is not to scale. Steps 1-3 in the above numbered list correspond to subfigure a); steps 4-7 to subfigure b); steps 8-9 to subfigure c); step 10 to subfigure d).

Here D is the particle diameter in units of μm. For estimating the additional scattering due to the dust deposited on the baffles, the superficial distribution of the fallout N is needed, as shown in eq.(2): this brings in a dependence on the exposure time t. The superficial cumulative distribution per unit area of particles of diameter $\geq D$ can be predicted by knowing the deposition velocity v_D :

$$N(D) = C_n \, v_D \, t \tag{4}$$

Particles deposit through different mechanisms in cleanrooms (gravitational, turbulent deposition, Brownian diffusion, and electrostatic attraction), also depending on the particle size. By fitting experimental data and theoretical arguments based on Stokes' law, the deposition velocity in an ISO8 cleanroom for cumulative particle sizes $\geq D$ is found [53] to be approximated as:

$$v_D = 2.02\,10^{-4} \cdot D^{1.656} \left[\frac{m}{s}\right] \tag{5}$$

For better cleanroom classes, the velocity of deposition is predicted to be larger, a factor 3 and 1.7 respectively in ISO Class 6 and 7 cleanrooms, at least for particles larger than 1μm. To make a prediction for ET we apply eq.s(4) and (5) with the mentioned correction factors: actually for simplicity the correction factor is applied to all diameters rather than just $D \geq 1\mu$m because this has negligible effect on the BRDF.

Fig.9-left shows the cumulative volumetric dust particle distribution expected in ISO6 and ISO7 clean rooms, and (right plot) the superficial density distribution of particles that have deposited. As for the exposure time, for each baffle, we assume here two possibilities: 1 hour and 10 hours. By exposure time we mean the time that runs from when the baffle seal is opened in the clean room (step 6 in the list of pag. 13) until the time when the section where it has been installed is attached to the already installed sections (i.e. step 9 in the list of pag. 13). To be on the safe side, for the superficial density we consider the pessimistic case of a baffle always oriented horizontally during the exposure time. To compare directly with the requirements of Tab.6, we use Fig.9-right to compute the number density of particles we expect to deposit on a baffle after 1 or 10 hours of exposure, for different size ranges and in different cleanroom classes: the results are shown in table 7. This shows that the baffle contamination during its handling in the clean room is negligible, even for 10 hours in ISO7.

We note here that differently from fig.9 the requirements are set assuming a flat distribution for each diameter bin. We also stress that our results are derived under the assumption of perfectly spherical particles. Finally as outlined above, a major source of uncertainty comes from the dust's index of refraction as well as from the particle deposition velocity eq.(5).

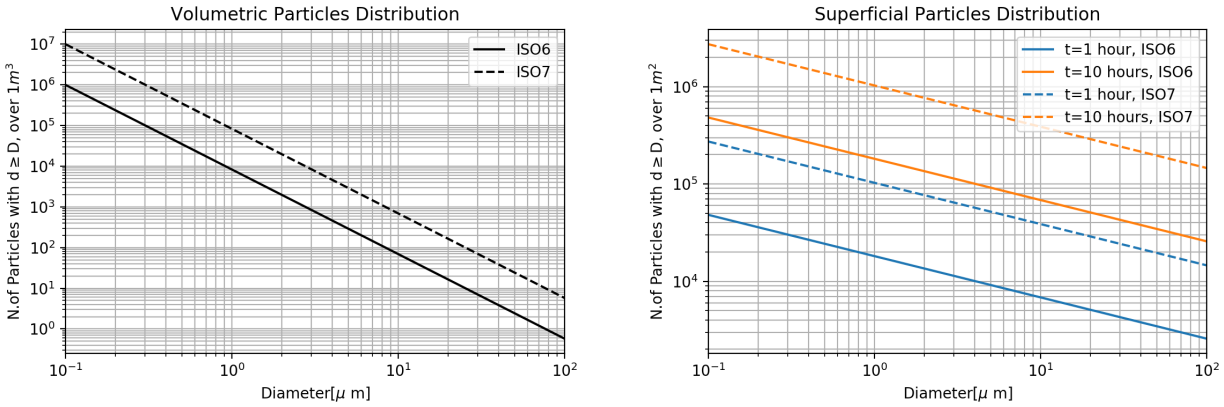

Figure 9: Left: cumulative volumetric dust particles distribution, according to eq.3. The solid and dashed curves correspond to ISO6 and ISO7 clean rooms. Right: cumulative superficial dust distribution deposited on a horizontal surface, following equation 4. Solid and dashed curves correspond to ISO6 and ISO7 clean rooms as in the left plot, while different colors correspond to different surface exposure times: 1 hour of exposure in blue, and 10 hours in orange.

	Density (particles/m^2)			
	1 hour		10 hours	
diameter range (μm)	ISO6	ISO 7	ISO6	ISO7
(0.1 - 0.3)	$1.8 \cdot 10^4$	$1.0 \cdot 10^5$	$1.8 \cdot 10^5$	$1.0 \cdot 10^6$
(0.3 - 1)	$1.2 \cdot 10^4$	$6.8 \cdot 10^4$	$1.2 \cdot 10^5$	$6.8 \cdot 10^5$
(1 - 3)	$6.8 \cdot 10^3$	$3.8 \cdot 10^4$	$6.8 \cdot 10^4$	$3.8 \cdot 10^5$
(3 - 10)	$4.6 \cdot 10^3$	$2.6 \cdot 10^4$	$4.6 \cdot 10^4$	$2.6 \cdot 10^5$
(10 - 30)	$2.5 \cdot 10^3$	$1.4 \cdot 10^4$	$2.5 \cdot 10^4$	$1.4 \cdot 10^5$
(30 - 100)	$1.7 \cdot 10^3$	$9.7 \cdot 10^3$	$1.7 \cdot 10^4$	$9.7 \cdot 10^4$

Table 7: Superficial density of particles expected to have deposited on a baffle after it is exposed horizontally for 1 hour or 10 hours in a clean room of ISO class 6 or 7. The range of particle size is shown in the first column.

As a general recommendation, we outline the importance that cleanliness procedures are followed in order for the ISO standard to be maintained also when people/machines are at work.

(c) Storage of pipe sections We consider now the contamination level reached when all particles deposit that were suspended in air within the pipe volume and that have entered the section when one of its ends was open and exposed to the clean room (subfigures b,c of fig.8. We consider that each section/baffle receives twice the same particle contamination: when it is the newly installed section and when it is the last section that has been installed already. In the following, we sum up these two identical contributions. The volumetric particle density is set by the ISO class of the clean tent used for welding the sections. We consider two cases: 1) the particles deposit uniformly on the surface of the pipe section, 2) the particles deposit only on the baffle surface. For case 1 we neglect the baffle's inclination angle and set its superficial particles density to be equal to that of the tube surface.

Table 8 shows the expected superficial number density of particles on the baffle surface in the different size bins, in the two cases of uniform distribution of particles on the section surface or particles deposited on the baffle only: the table shows the results for different ISO levels of the clean tent shown in fig.8. Comparing these results with the requirements of table 6, given all our hypotheses and approximations, we conclude that operation in ISO7 guarantees a large enough safe margin.

After that, the only contamination which remains to be accounted for is the one leftover from the cleaning process (item 3 in the above-mentioned list). We note that particles deposited on the upper side of the tube may at some point detach and cross the beam, contributing to stray light as discussed in sec.3.3.

Of course, should the process of pipe construction be different wrt what is outlined in paragraph a) at pag.3.1, we shall redo the computations accordingly. The requirements on the particle numbers shown in table 6 do not change.

We recommend to keep monitoring the amount of dust that accumulates in the assembled portion while this grows in time. In case the accumulated dust is found excessive, some extraordinary intervention could still be possible in the first steps of the assembly; alternatively, this monitoring will provide an estimation of the actual cleanliness level of the pipe and baffles, useful for estimating stray light noise. To monitor the cleanliness of the already installed portion of the pipe, the tube openings for the pumps can be exploited to place and retrieve any suitable device (e.g. particles counter).

	Density (particles/m^2)			
	uniform		concentrated	
diameter range (μm)	ISO6	ISO 7	ISO6	ISO 7
(0.1 - 0.3)	$4.5 \cdot 10^5$	$4.5 \cdot 10^6$	$5.6 \cdot 10^7$	$5.6 \cdot 10^8$
(0.3 - 1)	$4.7 \cdot 10^4$	$4.7 \cdot 10^5$	$5.9 \cdot 10^6$	$5.9 \cdot 10^7$
(1 - 3)	$3.7 \cdot 10^3$	$3.7 \cdot 10^4$	$4.7 \cdot 10^5$	$4.7 \cdot 10^6$
(3 - 10)	$3.9 \cdot 10^2$	$3.9 \cdot 10^3$	$4.9 \cdot 10^4$	$4.9 \cdot 10^5$
(10 - 30)	$3.1 \cdot 10^1$	$3.1 \cdot 10^2$	$3.9 \cdot 10^3$	$3.9 \cdot 10^4$
(30 - 100)	$3.2 \cdot 10^0$	$3.2 \cdot 10^1$	$4.1 \cdot 10^2$	$4.1 \cdot 10^3$

Table 8: Superficial density of particles expected to deposit on a baffle while the section where it is mounted is sealed (steps 10-11 in the list at page 3.1). We consider two cases: particles deposit uniformly on the whole section surface (columns 2,3) and particles that deposit only on the baffle surface (columns 4,5).

(d) Mechanisms that can introduce particles in the pipes under vacuum In addition to the fallout when baffles are in air, particles can accumulate also once the vacuum is closed: pumps operations, mechanical shocks on tube walls and opening/closing of gate valves can release particles.

A measurement of dust contamination in UHV is performed in ref.[11]:

- Ion pumps: particles are released only at ignition (pump started at a pressure $P_{ignition} = 10^{-5}$mbar) and no particles are emitted during operation. For a new pump, on average $N \sim 30$ particles are released. This number does not diminish along successive start/stop cycles; no data are given on the particles size.
- NEG pumps: Non Evaporable Getter (NEG) pumps with disks made by high-temperature sintering are found to be compatible with ultra-clean environments, due to their intrinsic very low dust release. Specifically, after some cycling no particles are detected in emission by the NEG pumps [12, 38].
- Gate valves: gate valves release particles when opened or closed. Over a 6 open-close cycle, $N \sim 2400$ particles are detected, 90% of them having diameter $D < 2\mu$m and 50% with $D < 0.5\mu$m. The number of particles released diminishes by half after 10 cycles, then remains constant up to 30 cycles.
- Shock on walls: particles are detected after the chamber or pipe walls are hit. After 5-10 shocks no more particles are released, but if the strength or place of impact is changed particles are released again. No quantitative data is reported which is useful to estimate the number or size of particles.

The number of pumps and gate valves in an ET arm is estimated using info in ref.[40]: here each arm will comprehend 30 gate valves, 30 NEG Pumps and 6 Ion Pumps. In addition, mobile pumping groups will be used during commissioning; 6 of them will be used per arm and they will be shared with neighbouring beampipes. From these numbers, we set an upper bound of $N_{\text{pumps}} \sim 50$ pumps and $N_{\text{gate valves}} \sim 75$ valves per pipe.

From the above number of pumps and the number of particles they release, we infer that the overall contamination by pumps is negligible (assuming they all contribute each as an ion pump).

Concerning the contamination due to gate valves, we consider 6 open-close cycles for each of the $N_{valve} = 75$ valves per arm: hence we estimate that about $2 \cdot 10^5$ particles would enter in each arm. If they deposit equally on the $N_{baffles} \sim 10^2$ baffles installed in each arm pipe, we expect $N \sim 2 \cdot 10^3$ particles (in the range $0.5\mu m < D < 2\mu m$) deposited on a single baffle. Here we note that particles might prefer to deposit on those baffles that are closest. We compare this number with the requirements of table 6. From this comparison, we conclude that the amount of particles expected by gate valves is respectively an order of magnitude below and similar to the particles expected after 1 hour in-air exposure respectively in ISO7 and ISO6 rooms. The contribution of particles released by gate valves is negligible if the baffles are exposed in air for longer periods.

Finally, we note that the above estimates of contamination from the vacuum system are likely pessimistic ones. First of all, we note that the measurements in [11] were made with no specific cleaning of the vacuum system. Furthermore, a reduction of the particles that can deposit on baffles can be achieved simply by attaching the elements of the pumping system to the lower side of the pipe or not in direct view of the pipe.

3.2 Requirements

In table 9 we report the requirements on beampipe deposited particles.

Cleanroom requirements during pipe assembly				
Requ. number	Name	Value	Units	Description
Req.1	maximum superficial particle density on the baffles, shown in tab.6			
Req.2	GatevalveDustnumber	400	#	Maximum number of particles released by gate valve (1 opening-closing cycle)
Req.3	GatevalveDustsize	2	μm	Maximum size of particles released by gate valve
Req.4	PumpDustnumber	30	#	Maximum number of particles released by pumps
Req.5	PumpDustsize	2	μm	Maximum size of particles released by pumps

Table 9: Requirements for scattering by deposited particles.

Recommendation 3.1: To reduce dust in the beampipe it is recommended to attach pumping systems to the lower side of the pipe.

Recommendation 3.2: The tube can not be left open during the storage phase, i.e. while modules are soldered together before completing and pumping a 5km section. Apertures must be sealed when not in use.

3.3 Dust crossing the beam

IN PROGRESS If we restrict ourselves to dust crossing the beam, a pictorial representation of the different scattering channels is reported in fig.10. Depending on the scattering angle (defined with respect to the beam axis) and the number of scattering events underwent by a photon, the main channels are:

1. **small-angle forward scattering**: Light is scattered in a forward direction and reaches the test mass (TM) which it was originally travelling to. This is represented as channel (1) in fig.10. Given the length of the ET arms, the scattering angle is small for most of the events (not for the ones close to the TM, which are however very few in percentage). The phase acquired with the scattering process can be exactly computed from Mie theory. However, the position of the dust particles along the pipe is random and therefore the phase of the light they scatter and reaching the TM is random too. We note that this channel includes the case of light transmitted by the particles.

2. **small-angle backward scattering**: Light is scattered in a backward direction and reach the same TM which it came from. This is represented as channel (2) in fig.10. Again, the scattering angle is small for most of the events (not for the ones close to the TM, which are however very few in percentage). The phase

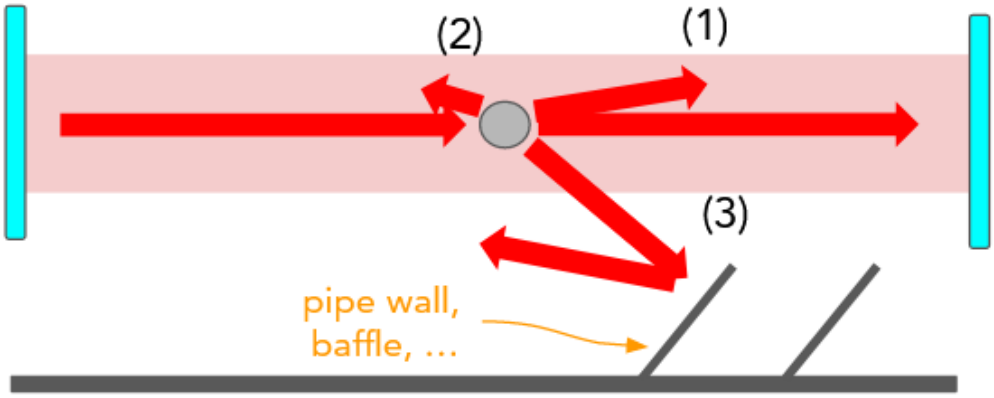

Figure 10: Pictorial representation of the possible scattering channels from dust particles crossing the beam. In this drawing, for clarity's sake, we restrict ourselves to consider the light travelling from TM1 (left light-blue rectangle) to TM2 (right light-blue rectangle). The possible scattering channels are three, as labelled in the drawing. (1): photons scattered at small angles and arriving to TM2. (2): photons back-scattered at small angles and arriving to TM1. (3) photons scattered at large angles and arriving to the baffles or pipe walls, where they are scattered again before going to a TM.

acquired with the scattering process can be computed exactly with the Mie theory. Again, for the same reason as above, the phase of the scattered light reaching the TM is random. We note that this channel includes the case of light specularly reflected by the particles.

3. **large-angle scattering**: Light which is scattered at large enough angles that it does not reach directly one of the TMs. Such light can reach the baffles or the beampipe walls, where it undergoes additional scattering. This channel diversifies in several cases:

   (a) Light scattered by a dust particle, reaching a baffle and being scattered to a TM

   (b) Light scattered by a dust particle, reaching a pipe wall and being scattered to a TM

   (c) Light scattered by a dust particle, reaching a baffle/wall, being scattered to another baffle/wall and eventually reaching a TM

   (d) ...

   For each of the cases listed, the physics involved is different (e.g. path length, acquired phase, the motion of the reached surfaces ...) and requires dedicated modelling and derivations (considering also that with increasing number of scattering events for light, the chances of reaching a TM decrease).

In the following, we restrict ourselves to scattered light reaching directly one TM as likely this arises the most relevant contribution.

We compute the strain noise generated by a set of particles with diameters extracted randomly from a given distribution, located at random positions along the beampipe ceiling $\vec{x_0}$ and detaching at a random time t_0. Once detached, particles are in free fall and along their trajectory interact with the main beam, whose intensity scales according to its Gaussian profile. We use Mie scattering to estimate the interaction of light with particles as in the previous section.

A Montecarlo code allows us to compute the field scattered towards a given point on the TM surface by the set of particles detaching from the beampipe. Hence we obtain maps of the scattered field on the TM surface: the projection on the main beam field is used to compute the strain noise.

3.4 Setting cleanliness requirements for tube walls

From the viewpoint of pipe manufacturing and construction it is often asked what the cleanliness requirements are for the pipe walls. Here we underline that the pipe walls are not seen directly by light, thanks to the baffles. So particles accumulated on the pipe are of concern only if later they fall on the baffles and/or cross the ET laser beam. There are 3 sets of requirements we can set for the beampipe surface cleanliness and which should all be satisfied:

- beampipe should be clean enough to be compatible with the clean room operation needed when installing the baffles. Vacuum experts can quantify the corresponding cleanliness requirement according to standard practice
- beampipe surface should satisfy the same cleanliness requirements as the baffles, and reported in table 6. In fact in vacuum as worst case we can assume that all dust on the pipe circular section in correspondence of a baffle has fallen on the baffle itself
- a requirement will come by quantifying the noise due to particles moving in vacuum inside the pipe and crossing the beam, see sec.3.3; our work will allow us to set upper limits on the rate and distribution of particles detaching from the pipe surface. Then by making some assumptions on the mechanisms that make the particle to detach we will be able to set requirements on the distribution of particles on pipe surface.

We cannot anticipate now what the combined effect of these 3 requirements will be. We propose that the cleanliness of the beampipe surface is considered as a parameter to be finalized at a later stage.

4 Beampipe pressure fluctuations. (A. Grado)

The vacuum system of ET, once assembled in the full configuration, will be among the largest UHV apparatus in the world. Assuming for the ET vacuum pipes, 1 m diameter and a total length of 120 km, the UHV volume will be $9.4 \times 10^4\ m^3$ with a beampipe inner surface of $3.8 \times 10^5\ m^2$. In the hypothetical case of adopting the Virgo solution to build it, the rough estimation of the cost is on the order of 560 million euros. In this scenario, the beampipe would consist of austenitic stainless steel (similar to AISI 304). However, this option appears impractical for ET as it necessitates a high-temperature thermal treatment to remove hydrogen from the bulk material. Due to these concerns, alternative approaches are being explored, including the use of ferritic steel. Initial findings indicate that other materials, typically not employed in ultra-high vacuum (UHV) applications, are appropriate for ET because they contain very low levels of diffusible hydrogen. A first evaluation of the requirements concerning the residual partial pressures in the beampipe was done in 2011 and is reported in the first conceptual design of ET. Here we report these values as reference: 10^{-10} mbar for H_2, 5×10^{-11} mbar for water and less than 10^{-14} mbar for hydrocarbons with molecular mass in the range of hundred and more. These values should guarantee a limit in terms of spectral strain sensitivity of ET due to residual gas fluctuations ranging around $10^{-25}\ 1/\sqrt{Hz}$.

The noise contribution to the sensitivity of a GW detector due to residual gas fluctuations in the UHV pipe arms is computed using the formula first derived in [41]:

$$S_L(f) = \frac{(4\pi\alpha)^2}{\nu_0} \int_0^{L_{tot}} \frac{\rho(z) e^{-2\pi f w(z)/\nu_0}}{w(z)} dz \tag{6}$$

where S_L is the power spectral density of the fluctuations of the optical path of a single arm of the interferometer, f is the frequency, α is the optical polarisability of the gas molecules, ν_0 is the average gas molecules speed, ρ is the molecules number density, $w(z)$ the laser beam radius, function of the arm coordinate, and L_{tot} is the interferometer arm length. Several experimental groups verified this formula by increasing the pressure in beam pipes interferometers and measuring the change in the sensitivity curve [55, 47, 37].

The general goal is to ensure the noise induced by pressure fluctuations inside the vacuum pipes remains at least a factor of 10 below the sensitivity curve of the planned ET-D detector design. In other words, we want a safety

margin of 10 at minimum. However, the exact level of vacuum system noise depends on multiple variables, such as the pumping speed and number of pumping stations, the specific gas composition inside the pipes, and the individual outgassing rates of each gas species. Due to these influencing factors, it's feasible to assume that achieving the desired 10-fold margin could be realized through diverse combinations, though it represents a formidable goal. The ultimate design, along with the specific partial pressure requirements for each gas species, will emerge from technical and economic optimizations, which are beyond the scope of this document.

For example, the noise values reported in Tables 10 and 11 for ET-HF and ET-LF respectively, were calculated assuming pumping stations every 500 meters with an effective gas-independent pumping speed of 5000 litres/second. The calculations specifically evaluated the noise at 23.9 Hz and 271.7 Hz, where the ET-D sensitivity curves reach their minimum for the low-frequency and high-frequency detectors, respectively.

At these critical frequencies, the safety margin ratios of actual ET-D sensitivity to total predicted gas fluctuation noise were approximately 19 and 9 for ET-LF and ET-HF respectively. Clearly, for ET-LF, we could relax the requirement on pumping speed or increase the distance among pumping stations to keep the factor 10 margin. This demonstrates it is plausible to stay within requirements through tuning factors like the pumping configuration and outgassing rate.

Gas species	Max pressure mbar	Noise HF $1/\sqrt{Hz}$	Margin
H_2	5.3×10^{-11}	1.7×10^{-26}	19
H_2O	9.6×10^{-12}	1.6×10^{-26}	20
N_2	5.6×10^{-12}	1.4×10^{-26}	23
CO	2.2×10^{-12}	1×10^{-26}	31
CO_2	2×10^{-12}	1×10^{-26}	26
$Hydrocarbon_{100}$	9.1×10^{-14}	1.5×10^{-26}	21

Table 10: Noise contribution to ET-HF due to residual gas fluctuations. The gas composition is supposed to be made of all the species listed in the table. The distance among pumps is assumed to be 500 m and the speed 5000 l/s (irrespective of the gas species). The ratio ET-D/total gas noise is 9.2. The margin in the right-hand column is calculated assuming that only the corresponding gas species is present in the beampipe. Among the gas species, it has been considered a generic hydrocarbon with molecular mass equal to 100 and polarizability of $15 \times 10^{-30}\ m^3$.

Gas species	Pressure max mbar	Noise LF $1/\sqrt{Hz}$	Margin
H_2	5.3×10^{-11}	2.1×10^{-26}	41
H_2O	9.6×10^{-12}	2.1×10^{-26}	42
N_2	5.6×10^{-12}	1.8×10^{-26}	48
CO	2.2×10^{-12}	1.3×10^{-26}	66
CO_2	2.0×10^{-12}	1.6×10^{-26}	55
$Hydrocarbon_{100}$	9.1×10^{-14}	2.1×10^{-26}	42

Table 11: Noise contribution due to residual gas fluctuations. The gas composition is supposed to be made of all the species listed in the table. The distance among pumps is assumed to be 500 m. The chosen specific outgassing, pumps capacity and distribution give a ratio ET-D/gas noise of 19.5 for ET-LF. The margin in the right-hand column is calculated assuming that only the corresponding gas species is present in the beampipe. Among the gas species, it has been considered a generic hydrocarbon with molecular mass equal to 100 and polarizability of 15×10^{-30} m^3.

As an example, we can report the average outgassing rate for H_2 according to the assumed pumping system distribution. The value is 1×10^{-14} $mbar\,l/s\,cm^2$ both for ET-HF and ET-LF. The calculation is performed solving the 6 numerically considering the pressure variation along the beampipe due to the finite conductance [23]. Table 12 illustrates that the requirements for ET on partial pressures are significantly more stringent than those for second-generation gravitational wave detectors, necessitating a substantial advancement in vacuum technology.

Gas pressure requirements				
Requ. number	Name	Value	Units	Description
Req.1	$PmaxH2$	5.3×10^{-11}	mbar	Maximum pressure for H_2
Req.2	$PmaxH2O$	9.6×10^{-12}	mbar	Maximum pressure for H_2O
Req.3	$PmaxN2$	5.6×10^{-12}	mbar	Maximum pressure for N_2O
Req.4	$PmaxCO$	2.2×10^{-12}	mbar	Maximum pressure for CO
Req.5	$PmaxCO2$	2.0×10^{-12}	mbar	Maximum pressure for CO_2
Req.6	$PmaxHydro100$	9.1×10^{-14}	mbar	Maximum pressure for hydrocarbon with molecular mass 100

Table 12: Requirements for the beampipe partial pressures assuming pumping stations with an effective speed of 5000 l/s (gas independent) placed every 500 m both for ET-HF and ET-LF.

5 Alignment and tolerances (M.Y. Barel)

This section applies to the triangle configuration

The goal of this section at this moment (march 2024) is to develop the terminology wherein tolerances can be discussed and set. On a informal note to understand the relevance: Outside this group working on beam pipe requirements, a other groups is working on the terminology of the coordinate systems. The influence of these choices are far reaching. Especially to its practical implementation. Industry and mechanical engineering has a profound understanding of this aspect which is more quickly overlooked in conceptual design phases. A first setup of, this here, is intended to give us a backbone to develop the alignments requirements and tolerance requirements as this section evolves. We need input from many disciplines on creating a total 'picture', to gather this, we need a general understanding and a reference frame. This section is still under construction. Any readers who think they have relevant information are invited to share this.

A tolerance stack-up analysis, often referred to as a "tolerance train", involves evaluating and calculating accumulated variations in dimensions and geometric features throughout the assembly and parts to determine whether they fall within acceptable limits or if they could potentially lead to problems such as interference, misalignment, or improper functioning of the final design.

The positioning of parts should be done in 6 degrees of freedom (DOF) for each part and connection. For this, we need a global coordinate system for all parts to refer to. The formulation of this needs to be discussed within the organisation.

As a first remark: The Einstein Telescope is so large that a chosen coordinate system is not aligned with the Earth's gravity vector at all given points. To this end a background document is being developed. (currently titled: "The implication of ET's Cartesian coordinate system in the spherical coordinate system of earth on civil slope's", and to be asked for at the Engineering department of the ETO, its not ready yet for release, march 2024) To give a general idea of the aspects: depending on the position of what part of ET is perpendicular to the gravitational vector of earth. The depth of parts of ET varies between 1.9 meters between parts or 7.8 meters between parts.

As a second remark is to answer the question: Does a laser on Earth follow a perfectly straight line, or does it bend to the earth's surface? Near the Earth's surface the bend of light due to the GR is very small, order of nano-radians. So from the perspective of the mirrors, the beam pipe is assumed completely straight.

These aspects are relevant to develop for example requirements on the slope for for example dewatering or stability of the mirror due to the tilt emerging from these geometric properties. Hence, putting an origin in one mirror or tower, is not leading to a axis that is parallel to other towers.

When a global coordinates system is chosen we can develop the tolerance trains. Below follow some proposed tolerance trains regarding the beamppipe.

The first tolerance train is cross-sectional to the tunnel and already described in the section about beam pipe radius, going from laser radius, r-offset, baffle, baffle connection offset, to beam pipe. But to complete it, it continues from the beam pipe to the support structure and goes to the tunnel wall. Added on top of all of this is the accuracy of the measurements themselves. In the current version (nov 2023) no margins are given between the baffles and the beampipe in the previous section. This is needed to determine the overlap between baffles and the scattered light, which in term formulates the undulation that the beampipe can have along 10 km. In this tolerance train, we also need estimates on tunnel sagging. The beampipe undulation will be at least limited by r-offset - baffle-beampipe margin.

This first tolerance train has 3 free DOF and 3 limiting DOF, defined as positioning X,Y (as just discussed) and rotation U. U doesn't seem obvious at first but can be imagined when two beam pipe sections need to align rotational-wise with for example the large section valves.

The second tolerance train is longitudinal to the tunnel and may be described by everything between the two mirrors in an interferometer arm. The straightness of the tunnel axis falles unther this tolerance and is essential to the requirement of the tunnel cross-sectional envelope.

The third relevant tolerance train might be the angle between the two arms of the interferometer. But if this is relevant needs to be assessed. A potential force of about 100 000 Newtons / meter is exerted on the ends of the beam pipe section. Although bellows might be used to absorb the strain in longitudinal direction this migh influence tower positioning too and with it the angle between 2 axis of the mirrors. From such cases requirements on beam pipe supports follow.

This section is still under construction. Any readers who think they have relevant information are welcome to share this.

6 Magnetic properties of the beampipe (E.Tofani, A. Grado)

There are many different possible magnetic noise sources in ET. These can be divided into two major categories: local and global sources. The latter are carefully studied in the global network of GWs antennas because they

can generate a noise source with a high correlation level. The network is not able to subtract this noise, which overlaps to the Stochastic Background of GWs (SGWB). Among these global sources, the *Schumann resonances* represent one of the most important.
In the context of local sources, in this section we will analyse the possible noise generated by the magnetic field due to the residual magnetisation of the beampipe material [2][26].

6.1 Magnetic dipole model

The general aim of this section is to describe the coupling of a ferritic steel beampipe with the magnets glued on the mirrors of ET. Indeed, it is necessary to quantify the magnetic noise introduced by the beampipe itself in the hypothesis it will be made of this kind of steel. A reasonable starting point is to consider the main contribution to this magnetic noise on the laser beam direction. Therefore, in our model, we can properly place the ferritic beampipe at a distance z from one of the mirrors in the longitudinal direction. We also divide the tube in infinitesimal rings to simplify our analysis (Fig.11).
The further analysis is based on the Ampère's equivalence theorem applied to a dipole magnetic moment $\vec{m}$. In the surrounding environment $\vec{m}$ generates a field $\vec{B_0}$. Therefore, we can describe the coupling strength which set up between two permanent magnets as follows. Let $\vec{m}_1$ be the dipole moment of one ring of tube and $\vec{m}_2$ the one of the magnets glued on the surface of the mirror. Actually, the notation $d\vec{m}_1$ instead of $\vec{m}_1$ in our analysis is more formally correct. Consequently, the strength acting on the second magnet is [36]:

$$d\vec{F}(z) = |\vec{m_2}| \frac{d}{dz} B_0(z)\,\hat{z} = -\frac{3\,\mu_0}{4\,\pi} \frac{|d\vec{m}_1|\,|\vec{m}_2|}{z^4} \left[1 + 3\cos^2\theta\,(\hat{m_1})\right]^{\frac{1}{2}} \hat{z} \tag{7}$$

where $\theta(\hat{m_1})$ is the angle between $\hat{z}$ and the dipole moment of the ring of tube (Fig.11).
The beampipe will form a comoving system to the floor. For this reason, we also make the hypothesis that, in first approximation, it vibrates according to the seismic noise. Since the beampipe moves, the distance $z(t)$ between the element of beampipe and the mirror changes. We take into account of the distance l between one

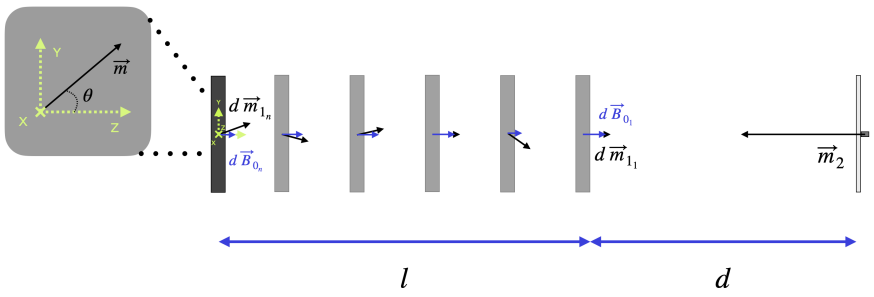

Figure 11: Representation of the subdivision of the beampipe in the magnetic dipoles model: each ring of tube has a magnetic dipole moment $d\,\vec{m}_{1n}$ and gives a contribution $d\,\vec{B}_{0n}$ to the coupling with the magnets of the mirror. Only one mirror is designed for simplicity

ring of tube and the magnet glued to the mirror together with the longitudinal displacement due to the seismic vibration $\delta z(t)$:

$$z(t) = l + \delta z(t)$$

In the present model we are considering ferritic steel as the material for the beampipe. We know that the magnetic dipole of a generic ferritic beampipe might be calculated considering the typical values of the normal coercive force F_c. We might write it as the ratio: $F_c(|\vec{m}_1|) = |d\vec{m}_1|/dV_T$ where $dV_T = 2\pi r\,\Delta r\,dl$ is the infinitesimal volume of tube. Actually, not the whole beampipe is ferritic. Indeed, the cryotraps cannot be made of this steel. It means that when we integrate over all the rings, we should not consider any ferritic tube at a distance lower than $z = d$. In particular, for both the LF interferometer and the HF one, this distance is $d = 10\,\mathrm{m}$ [45]. Therefore, if F_c and θ weakly depend on the changes of the magnetic dipole along the beampipe, the problem might be solved as follows. In ET the mass of a mirror will be $M = 200$ kg [45]. It follows that

the acceleration of the whole beampipe can be written as:

$$\vec{a}(z) \sim -\frac{\mu_0}{2}\frac{F_c\, r\, \Delta r\, |\vec{m}_2|}{M}\,(1+3\cos^2\theta)^{1/2}\frac{1}{(d+\delta z)^3} \tag{8}$$

To calculate the PSD of the magnetic noise due to the beampipe, it is useful to write the general equation for the PSD of the acceleration:

$$PSD(\vec{a}) = (2\pi f)^4\, PSD(\vec{z}) \tag{9}$$

Calling

$$C = -\frac{\mu_0}{2}\frac{F_c\, r\, \Delta r\, |\vec{m}_2|}{M}\,(1+3\cos^2\theta)^{1/2}$$

and using the equation (9) we will calculate the magnetic PSD as follows:

$$PSD(\vec{z}) = \frac{1}{(2\pi f)^4}\frac{9C^2}{d^8}\,PSD(\delta z) \tag{10}$$

Since the data from Sos Enattos are velocities, we should write the $PSD(\delta z)$ as follows:

$$PSD(\delta z) = \frac{PSD(\delta v)}{(2\pi f)^2} \tag{11}$$

Calling $S_v(f)$ the seismic Power Spectral Density in Sos Enattos, using the previous relation (11), we will write the PSD (10) as:

$$S_z(f) = \frac{1}{(2\pi f)^6}\left[-\frac{3\mu_0}{2}\frac{F_c\, r\, \Delta r\, |\vec{m}_2|}{M}\,(1+3\cos^2\theta)^{1/2}\right]^2\frac{S_v(f)}{d^8} \tag{12}$$

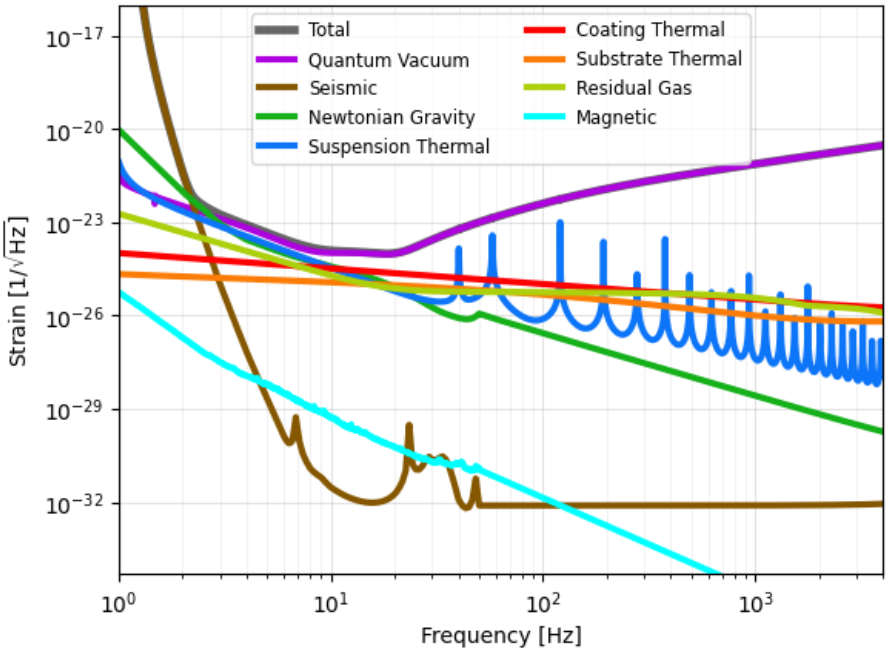

Figure 12: Magnetic strain noise in ET-LF Sos enattos with a distance tubebeampipe-mirror $d = 10\,\mathrm{m}$. The noise refers to ferritic, whose magnetic properties are acquired by the permagraph method ($F_c = 400\,\mathrm{A/m}$ [34]). This magnetic curve is calculated setting $\theta = 0$.

Magnetic requirements on beampipe material				
Requ. number	Name	Value	Units	Description
Req.1	F_c	$300 \div 400$	A/m	normal coercive force

Table 13: Requirements on the magnetic properties of the beampipe material.

The coercive force (F_c) is defined in the cycle of hysteresis in the point where the magnetic induction vector $\vec{B}$ is set to zero. Usually, measurements of F_c are performed following three steps. Firstly, the steel is demagnetized in order to cancel the previous history of magnetization. Secondly, the initial magnetization curve is recorded until the steel reach the saturation and finally, the magnetic induction vector $\vec{B}$ is set to zero. Therefore, in this model a demagnetization of the ferritic steel of the beampipe should be considered just to establish a reference value of the coercive force.

7 Surface hydrocarbon contamination (E. Tofani)

To test the hydrocarbon contamination RGA and X-ray Photoelectron Spectroscopy (XPS) analysis are commonly used together with the FTIR (Fourier Transform Infra Red) spectroscopy. The LIGO collaboration commonly uses only the last one for components too large to fit in the UHV bake oven [10]. Generally, with the FTIR instrument is easier to distinguish molecules than using the XPS.
Quantitative FTIR measurements of the non-volatile residue (NVR) are necessary to verify if the amount of residue meets the contamination requirements. Generally, the results are expressed in $\mu g/cm^2$ for surfaces and μg/hole for threaded holes.
The wavenumber of an IR adsorption spectra ranges from $\sim 400\,cm^{-1}$ to $\sim 4000\,cm^{-1}$. Moreover, following the LIGO collaboration [10], it is possible to define the specific absorption z at a wavenumber of interest in order to quantify the absorption of the contaminant in the solvent. Therefore, z can be calculated as follows:

$$z = \zeta \left(ln(I/I_0)_{sample} - ln(I/I_0)_{ref} \right) \tag{13}$$

with

$$\zeta = \frac{A_w\, V_s}{A_s\, V_e} \tag{14}$$

In the equation (13) I_0 indicates on the one hand the background of the chamber of the instrument (I_{0s}), on the other hand, the background of the reference for the sample (I_{0r}). Once the procedure has been fixed, the relation (14) can be considered as a typical constant of the process. Indeed, A_w is the area of the FTIR window while A_s is the analysed surface of the sample. V_e represents the volume of the solvent evaporated onto the window and V_s the volume of the solvent sample. The constant can be calculated considering two different procedures like the one used by LIGO ($1.06 \cdot 10^{-4} \leq \zeta_L \leq 3.18 \cdot 10^{-4}$) and that followed at CERN ($\zeta_C = 7.213$).
Using a FTIR analyser it is possible to see the absorption line due to the molecular stretch of the CH_2 and CH_3 bounds, which we can find in hydrocarbons. In particular, to evaluate the hydrocarbon contamination, we can calculate the specific absorption at $2950\,cm^{-1}$. This is the wave number of the deepest hydrocarbon absorption line. The goal for the UHV system in ET is to set a threshold value for the hydrocarbon specific absorption z_{2950}, which should be compatible with the maximum pressure $p_{hy} = 1 \cdot 10^{-14}\,mbar$.
However, there is an unavoidable exposition of samples to air, which contaminates the surface of metals. In particular O, C and N, in addition to water vapour, can be absorbed during the exposition. For this reason, the Surfaces, Chemistry and Coatings (SCC) laboratories at CERN had fixed a threshold for any UHV system ($p < 10^{-9}\,mbar$). More precisely, they measured the *surface atomic concentration* ($at.\%$) of the carbon amount on the surface of the metal through the XPS technique. For stainless steel it resulted the value [27][32]:

$$C = 31.3\,at.\% \tag{15}$$

Following the CERN procedure, a sample with the level of contamination (15) can be used as a reference for the FTIR technique fixing the threshold for the desired molecule. In particular, the document [7] about the

FTIR test at SCC establishes that, if the area between the line at $2950\,cm^{-1}$ and the reference spectrum of the window gives a value ≤ 0.02, the sample is considered acceptable for UHV.
Moreover, thanks to this measurement of the carbon concentration, in principle it could be possible to evaluate the outgassing rate level compatible with the maximum pressure of hydrocarbons in a UHV system. Indeed, once established the threshold for air exposure, with the same samples we could measure the specific outgassing rate at the desired pressure and obtain a further cross-check, in addition to the FTIR analysis. Therefore, it is possible to decide a standard procedure to test the surface cleanliness of the vacuum parts in ET. In general, it is necessary to note that whatever is the level of UHV, the carbon concentration is always affected by the air contamination. Therefore, if a lower threshold for the level of hydrocarbon contamination, compatible with the low pressure p_{hy} in ET, was necessary, it might be fixed only by including the RGA analysis.
The procedure used at CERN SCC for the FTIR technique is described in the document [7].

As outlined in this section, hydrocarbon contaminants pose challenges in both detection and quantitative measurement. It's crucial to minimize the risk of accidental contamination, which, in practice, cannot be easily remedied, particularly with bake-outs at temperatures as low as 80Â°C. Therefore, the use of lubricants in any components that might come into contact with the beampipes should be avoided, except in exceptional circumstances that require specific authorization.

Hydrocarbons contamination requirements				
Requ. number	Name	Value	Units	Description
Req.1	ζ	7.213	-	CERN procedure
Req.2	z	$< \sim 2.1$	-	specific absorption
Req.3	$at.\%\,C$	< 31.3	-	carbon surface contamination level in XPS

Table 14: Requirements on beampipe inner surface hydrocarbons contamination.

8 Pumpdown time (J. Gargiulo, C. Scarcia)

The pump-down time is intended as the maximum time needed from the start of the rough pumping to reach the maximum pressure in which the interferometer is operational. The stages that compose the pump-down, as intended here, are:

- Rough pumping,
- High Vacuum (HV) pumping,
- Bake-out,
- Ultra High Vacuum (UHV) pumping.

The whole pump-down procedure is considered a special operation to be performed once and only for the initial commissioning of the beam pipes.
Each 10 km long interferometer arm is assumed to be divided into 5 km long sectors by large gate valves. The gate valve presence would help ease the bake-out energy requirement and give flexibility in case of significant issues (i.e. large leak that requires cutting and re-weld of a section) without breaking the vacuum on an entire arm. The valve position might be shifted in the final configuration to reduce the gas load induced by the gate valve's presence on the residual gas noise, especially near a critical point where the laser beam is at its minimum waist. All the considerations that will follow are going to be based on a five km-long sector.

The prerequisites for starting the pump-down operations are beam pipes already installed, aligned, covered with suitable insulation, and the butt welded joints leak-tightness checked.
A tight vacuum system is necessary to ensure an ultimate pressure within the prescribed values and limit the accumulation of poorly gaseous gases like Argon. A subsequent step will specify the acceptable air leak rate for each component, section, and the interferometer as a whole prior to installation and during operation. It is important to remember that leak testing all welds of the beam pipe and flanged components will impact both time and cost. The strategy and methods for leak testing, as well as the maximum leak rates accepted, will be

a key consideration at CERN.
Currently, there is no plan to initiate with a higher beampipe pressure during the start-up phase, such as for the pre-commissioning of the LF interferometer with the cryogenic towers at room temperature.

Rough pumping

Rough pumping is one of the most delicate and time consuming operations. In this stage, the entire sector volume is meant to be emptied, and the pressure is brought from 1 bar to a value of a few tenths of mbar (pressure low enough to start the turbo-molecular pumps). The rough pumping could be done with high pumping oil-free root pump (backed by a screw pump) mounted on one extremity of the sector.
Suppose we assume a pumping speed of 1000 $m^3 \cdot h^{-1}$, the rough pumping should take from 4.5 up to 10 days to go from 1 bar to 1E-1 mbar, whether the pump is directly mounted on the vacuum system or in the case is connected through a flexible hose to the sector. The pressures reported above should be intended to be reached at the opposite extremity where the pump is mounted.

High Vacuum pumping

The high vacuum pumping can be started at 1E-1 mbar and extended to 1E-6 mbar. Going beyond 1E-6 mbar will not result in significant pressure reduction gain after the bake-out nor time shortening the bake-out itself. **Reaching the low 1E-6 mbar range between the HV pumps should not take more than 15 days.** During the HV pumping, it should be possible to monitor the level of water vapour and contaminants present in the residual gas, which can be used to drive the bake-out duration.

Bake-out

Once reached the low 10^{-6} mbar range, the bake-out can be initialized. The bake-out ramp rate is advised to be between 2 and 5°C/h to ensure temperature uniformity and stability in power absorption. Distributed NEG pumps can be an excellent option for exploiting their high pumping speeds for water vapour to accelerate removal. The duration of the bake-out itself is directly proportional to the temperature at which the treatment is done and how serrated is the NEG distribution. Given a temperature domain between 80°C and 150°C, the duration of the bake-out could range from 7 to 30 days. Passed the bake-out duration, the sector can be cooled down between 2 and 5 °C/h.

UHV pumping

Mass scans should be performed one to two days after the sector has been cooled down to the tunnel temperature. In the absence of leaks, the sector can be considered ready. If leaks are detected, or major issues happen, the additional time has to be evaluated at the moment according to the severity of the repair and the time for the re-commissioning.

The pump-down time before a sector is ready for operation is then calculated as follows:

$$\begin{aligned} t_{\text{pump-down}} = t_{\text{Rp}} + t_{\text{HVp}} + (T_{\text{bake-out}} - T_{\text{tunnel}})/\alpha_{\text{bake-out}} + \\ + t_{\text{bake-out}} + (T_{\text{bake-out}} - T_{\text{tunnel}})/\beta_{\text{cooling}} + t_{\text{UHV scan}} \end{aligned} \tag{16}$$

Where:

- t_{Rp} = Rough pumping time in days.
- t_{HVp} = High Vacuum pumping time in days.
- $\alpha_{\text{bake-out}}$ = Bake-out ramp rate in °C/day.
- $T_{\text{bake-out}}$ = Bake-out temperature °C.
- T_{tunnel} = Tunnel temperature °C.

- $\beta_{\text{bake-out}}$ = Bake-out cooling rate in °C/day.
- $t_{\text{UHV scan}}$ = time needed at UHV regime before taking the last scan before delivering the sector in days.

Given the consideration mentioned earlier, assuming for example, a bake-out temperature range from 80°C 150°C and a tunnel temperature of 20°C, one can calculate the maximum and minimum pumpdown time:

- t_{Rp} = 4.5 - 10 days.
- t_{HVp} = 7 - 15 days.
- $\alpha_{\text{bake-out}}$ = 120 - 48 °C/day (5 - 2°C/h).
- $t_{\text{bake-out}}$ = 7 - 30 days
- $\beta_{\text{bake-out}}$ = 120 - 48 °C/day (5 - 2 °C/h).
- $t_{\text{UHV scan}}$ = 2 days.

The minimum and maximum pump-down time for one 5 km long sector are 22 - 62 days.
As to be remarked that the pump-down time is calculated for a leak/major issue-free scenario, any delay to the beam pipe commissioning time has to be evaluated at the moment according to the severity of the repair and the time for the re-commissioning.
The vacuum system must be equipped with venting valves in case the pressure has to be brought to atmospheric levels. Dry air is advised to vent the sections to limit the humidity entering and fasten the recovery pumpdown operation. The venting equipment must also incorporate dust filters to prevent dust from entering the beampipe.

Pump down				
Requ. number	Name	Value	Units	Description
Req.1	Tpumpdownmax	62	days	Maximum pumpdown time assuming a bakeout temperature of 80 deg
Req.2	drypumps	-	-	all the pumps used must be dry.
Req.3	dustfree	-	-	pumps must be free of dust or proper dust filters must be used

Table 15: Requirements on beampipe pump down time.

8.1 Lifetime

The beampipe vacuum system is required to have a minimum operational lifespan of 50 years. This implies that any component of the system that cannot be replaced without venting must possess a lifespan exceeding 50 years or be mounted with a gate valve in front.

9 Interface requirements

9.1 Maximum allowed temperature in the tunnels. (P. Werneke, M.Y. Barel)

This section applies to both configurations.

The first orientation on the maximum temperature allowed in the tunnels during bake-out indicates that human working conditions are limiting the maximum temperature. Other aspects of influence on the bake-out conditions may be the tunnel concrete temperature and the temperature difference over the concrete wall. Tunnel temperature limitations based on electronics or machinery are kept out of scope assuming they exceed the human working conditions.

The Dutch government [50] indicates that when temperatures are above 26 °C employers need to think about actions that can be taken to ensure employees' health. For intense physical work, the indicated limit is 26 °C, for office work it is indicated to be 28 °C. This is regardless of the humidity conditions. However, the tunnel humidity can be expected to be of influence. (Limited to 60 % humidity 9.2) And therefore we need to take into account the so-called perceived or apparent temperature. The table below illustrates the correlation between relative humidity and air temperature.

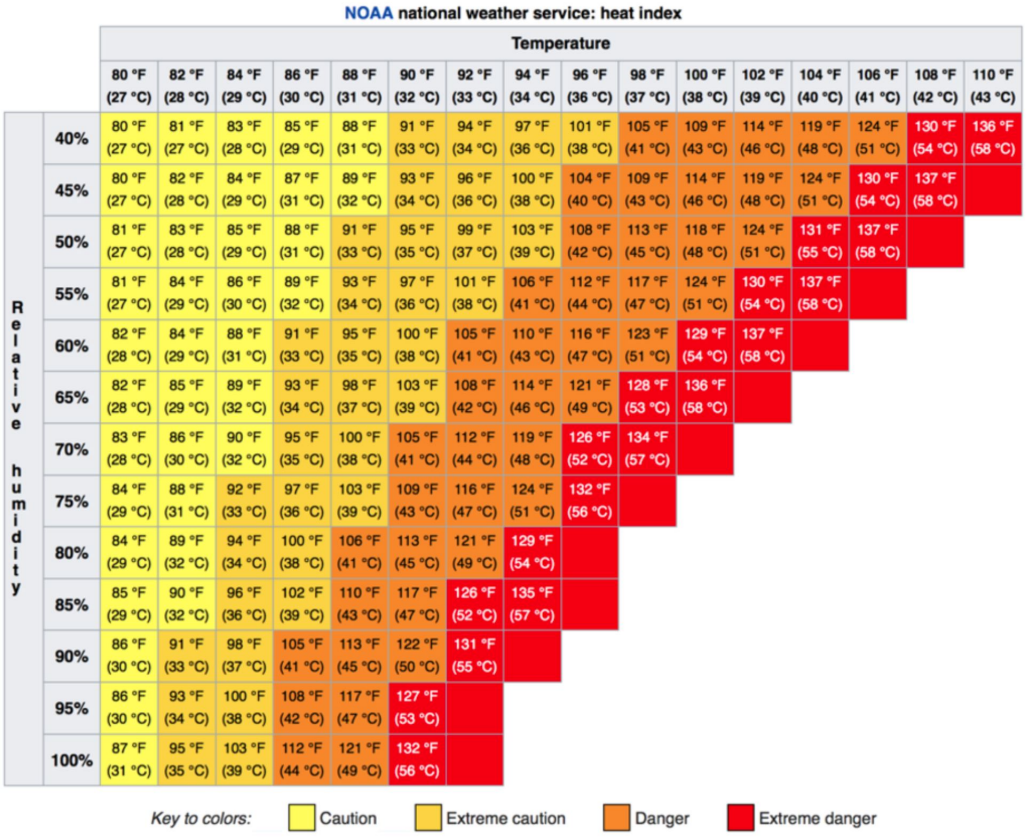

Relative humidity	80 °F (27 °C)	82 °F (28 °C)	84 °F (29 °C)	86 °F (30 °C)	88 °F (31 °C)	90 °F (32 °C)	92 °F (33 °C)	94 °F (34 °C)	96 °F (36 °C)	98 °F (37 °C)	100 °F (38 °C)	102 °F (39 °C)	104 °F (40 °C)	106 °F (41 °C)	108 °F (42 °C)	110 °F (43 °C)
40%	80 °F (27 °C)	81 °F (27 °C)	83 °F (28 °C)	85 °F (29 °C)	88 °F (31 °C)	91 °F (33 °C)	94 °F (34 °C)	97 °F (36 °C)	101 °F (38 °C)	105 °F (41 °C)	109 °F (43 °C)	114 °F (46 °C)	119 °F (48 °C)	124 °F (51 °C)	130 °F (54 °C)	136 °F (58 °C)
45%	80 °F (27 °C)	82 °F (28 °C)	84 °F (29 °C)	87 °F (31 °C)	89 °F (32 °C)	93 °F (34 °C)	96 °F (36 °C)	100 °F (38 °C)	104 °F (40 °C)	109 °F (43 °C)	114 °F (46 °C)	119 °F (48 °C)	124 °F (51 °C)	130 °F (54 °C)	137 °F (58 °C)	
50%	81 °F (27 °C)	83 °F (28 °C)	85 °F (29 °C)	88 °F (31 °C)	91 °F (33 °C)	95 °F (35 °C)	99 °F (37 °C)	103 °F (39 °C)	108 °F (42 °C)	113 °F (45 °C)	118 °F (48 °C)	124 °F (51 °C)	131 °F (55 °C)	137 °F (58 °C)		
55%	81 °F (27 °C)	84 °F (29 °C)	86 °F (30 °C)	89 °F (32 °C)	93 °F (34 °C)	97 °F (36 °C)	101 °F (38 °C)	106 °F (41 °C)	112 °F (44 °C)	117 °F (47 °C)	124 °F (51 °C)	130 °F (54 °C)	137 °F (58 °C)			
60%	82 °F (28 °C)	84 °F (29 °C)	88 °F (31 °C)	91 °F (33 °C)	95 °F (35 °C)	100 °F (38 °C)	105 °F (41 °C)	110 °F (43 °C)	116 °F (47 °C)	123 °F (51 °C)	129 °F (54 °C)	137 °F (58 °C)				
65%	82 °F (28 °C)	85 °F (29 °C)	89 °F (32 °C)	93 °F (34 °C)	98 °F (37 °C)	103 °F (39 °C)	108 °F (42 °C)	114 °F (46 °C)	121 °F (49 °C)	128 °F (53 °C)	136 °F (58 °C)					
70%	83 °F (28 °C)	86 °F (30 °C)	90 °F (32 °C)	95 °F (35 °C)	100 °F (38 °C)	105 °F (41 °C)	112 °F (44 °C)	119 °F (48 °C)	126 °F (52 °C)	134 °F (57 °C)						
75%	84 °F (29 °C)	88 °F (31 °C)	92 °F (33 °C)	97 °F (36 °C)	103 °F (39 °C)	109 °F (43 °C)	116 °F (47 °C)	124 °F (51 °C)	132 °F (56 °C)							
80%	84 °F (29 °C)	89 °F (32 °C)	94 °F (34 °C)	100 °F (38 °C)	106 °F (41 °C)	113 °F (45 °C)	121 °F (49 °C)	129 °F (54 °C)								
85%	85 °F (29 °C)	90 °F (32 °C)	96 °F (36 °C)	102 °F (39 °C)	110 °F (43 °C)	117 °F (47 °C)	126 °F (52 °C)	135 °F (57 °C)								
90%	86 °F (30 °C)	91 °F (33 °C)	98 °F (37 °C)	105 °F (41 °C)	113 °F (45 °C)	122 °F (50 °C)	131 °F (55 °C)									
95%	86 °F (30 °C)	93 °F (34 °C)	100 °F (38 °C)	108 °F (42 °C)	117 °F (47 °C)	127 °F (53 °C)										
100%	87 °F (31 °C)	95 °F (35 °C)	103 °F (39 °C)	112 °F (44 °C)	121 °F (49 °C)	132 °F (56 °C)										

Figure 13: Heat index showing apparent temperatures at relative humidity and air temperatures [25]:

During bake-out, it is assumed that no people are in the tunnels. But in cases of emergency or high needs, humans need to be able to do short-term activities, we accept therefore the caution level as the highest limit. This then leads to the maximum allowable air temperature in the tunnel of 29 °C during bake-out.

Regarding the concrete temperature. We estimate that the maximum concrete operational temperature is at 65 °C. A literature review from 2005 on the effect of elevated temperatures on concrete materials and structures [35], refers to the maximum allowable temperature of 65 °C in the American Society of Mechanical Engineers Pressure Vessel and Piping Code. It is advised to investigate this further as this might be very different for the tunnel concrete sections. Nonetheless, this will not be the limiting factor for the maximum allowable tunnel temperature.

As for the temperature difference over the inner and outer surface of the concrete, it is estimated that the lower range of this can be 15-20 °C. This is based on a rule of thumb stated by the Beton Lexicon website (and refers to NEN norms for further information) [33]: indicating this aforementioned temperature difference during concrete hardening. This can be used as a conservative requirement until better estimations are found. This jet again depends on the design choices made. Combining the maximum air temperature to be 29 °C, and a soil temperature of around 15 °C, also leads to a temperature difference in the same range.

Concluding in two requirements:

Maximim allowed temperature in the tunnels				
Requ. number	Name	Value	Units	Description
Req.1	Tunnel Air temperature during bake-out	<30	°C	restricted acces.
Req.2	Tunnel Air temperature standard maximum	<26	°C	normal access.

Table 16: Requirements on the maximum temperature allowed in the tunnels.

9.2 Maximum allowed relative humidity level in the tunnel. (M.Y. Barel)

This section applies to both configurations

The causes of moisture in tunnels are first described. We formulate a limit based on what electronics can handle.

The moisture level in the tunnel is dependent on the soil type, the humidity influence of the ventilation system, and the type of construction. Groundwater penetration through the coating of the layer can best be estimated after the site has been chosen.

An assessment report from Implenia about the scope of work for the civil engineering scan for the South Limburg Border region [22], assumes a long-term inflow of water in the range of some tens of liters per second for the overall construction for cost assessments.

But mo(i)st influential, residual construction water from the tunnel boring machining may cause the majority of the humidity during the first two years. A Review of Ventilation and Environmental Control of Underground Spaces [29] states that tunnel humidity can reach 95 % relative humidity within the first two years of construction. Health measures might be needed as another study [54] indicates the consequences of ventilation (and humidity) in subway stations.

A point of concern is the dew point. Mark G. Lawrence proposed a simplified formula in 2005 [28] that describes a simplified equation relating observed temperature (in degrees Celsius) and relative humidity to the dew point temperature.

$$T_{\mathrm{d}} = T - ((100 - RH)/5) \tag{17}$$

We assume that at a depth of 10 meters, the temperature of the soil can be estimated to be 10 °C. Every 100 meters the temperature of the soil rises with 3 °C. At 250 meters depth, we estimate the temperature to be between 15-20 °C. A borehole in Sardinia shows a temperature of around 18 °C [1]

A bake-out scenario with higher temperature extremes and therefore higher likelihood of condensation is the following: If we assume that the dew point temperature needs to stay above 20 °C, to prevent condensation on the tunnel wall, and the tunnel temperature to be 29 °C. Then we can only allow for a humidity of 65 %.

Besides that scenario, the standard comfort range for people to work is between 40 - 60 %.

Therefore, max. allowed relative humidity level in the tunnel is set to 60 %. From the equation, it also follows that at 60 % the temperature differences for, for example, electronics and other sensitive equipment cannot be more than 8 °C below the tunnel air temperature.

Humidity				
Requ. number	Name	Value	Units	Description
Req.1	max. tunnel Humidity	60	%	
Req.2	max. temperature difference to water sensitive objects	8	°C	applicable: object T < environment T

Table 17: Requirements on the humidity in the tunnels.

9.3 Maximum allowed acoustic noise in the tunnels. (T. Bulik)

In this section, we will outline the possible influence of the acoustic noise on the beampipes and their possible vibrations. We will assume a simple geometry where the beampipes have a diameter of $D_{pipe} = 1$m, and they are placed in a tunnel with a diameter of $D_{tunnel} = 8$m. The tunnel diameter plays little role in the calculation.

The sound waves in a tunnel will propagate in all directions. The pressure force on the beampipe will be exerted only by the component of the wave that is perpendicular to the tunnel and pipe.

Let us assume that the velocity of the sound waves is $v = 330\,\mathrm{m\,s^{-1}}$, and denote their frequency as f. The wave vector $\vec{k}$ can have any direction. The sound wave will have an amplitude of the pressure p_0 and can be described as:

$$p(\vec{r}, t) = p_0 \sin(\vec{k}\vec{r} - \omega t + \varphi) \tag{18}$$

and we choose a coordinate system centred on the beampipe in which the pipe goes along the Y axis, and the Z axis is vertical. Let us first consider the case of a monochromatic wave propagating in the direction $\vec{n}$, and we calculate the force in the direction X.

The amplitude of the force of the pipe per unit length per unit pressure amplitude will be

$$\mathcal{T}_x(f) = \frac{1}{p_0}\frac{dF_x}{dl} = \frac{D_{pipe}}{p_0}\int d\phi p(\vec{R}_\perp(\phi), t = 0)\cos\phi \tag{19}$$

where ϕ is the angulr coordinate of the pipe surface, and $\vec{R}_\perp(\phi) = D_{pipe}(\sin\phi, 0, \cos\phi)$ is a vector describing surface of the pipe at $y = 0$. In general, the wave field will not be monochromatic. We can analyze two cases: isotropic field and semi-isotropic one. For the semi-isotropic case, we assume that waves with a wavelength that does not fit into the tunnel will be suppressed. We calculate the mean force per unit length per unit pressure by averaging its square over all directions and phases:

$$\mathcal{T}_x^{mean}(f) = \left(\langle \mathcal{T}_x^2(f)\rangle_{\vec{n},\varphi}\right)^{1/2}. \tag{20}$$

The calcuation is analogos for the force in the z direction. The force vanishes in the Y direction (along the pipe).

We present the force per unit length and per pressure amplitude in Figure 14. The maximum of the transfer function corresponds to the frequency for which the width of the beampipe corresponds to the length of the wave $f_{max} \approx v/(2\pi D_{pipe})$. In the case of the semi-isotropic field, there is another characteristic frequency of approximately 20Hz. This corresponds to the regime where in the case of semi isotropic field some waves are suppressed because of the dimensions of the tunnel.

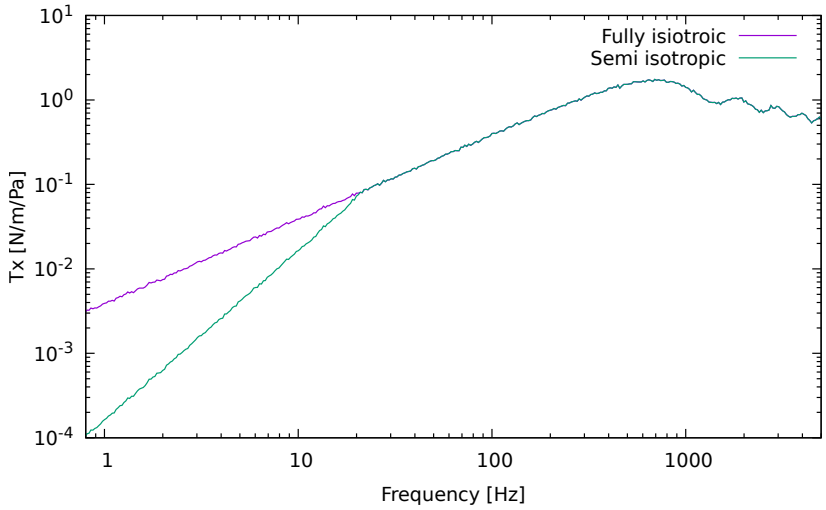

Figure 14: Transfer function between the pressure amplitude and force on the beampipe per unit length. We present the isotropic and semi-isotropic wavefield.

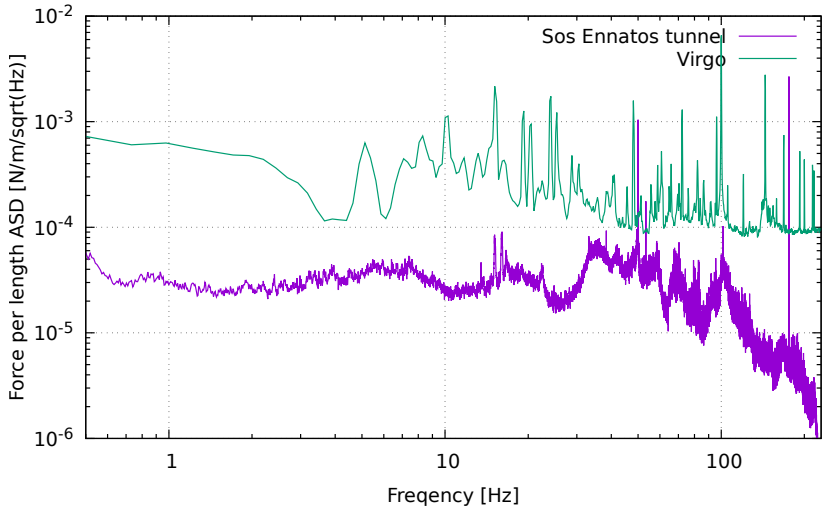

Figure 15: The spectral amplitude of the force per unit length of the beampipie calculated assuming the level of noise at Virgo (green line) and in the Sos Ennatos tunnel (violet line).

Let the sound amplitude spectrum be $\tilde{p}(f)[\mathrm{Pa\,Hz^{-1/2}}]$. Then the spectrum of the force acting on a fraction of the beampipe with length L will be

$$\tilde{F}(f) = T(f)L \times \tilde{p}(f) \tag{21}$$

We can now present the resulting force per unit length based on two examples of measured infrasound spectra. This is the case of the tunnels of the Sos Ennatos mine which are very quiet, and from the central building of Virgo. The two cases will bracket the expected level of noise and therefore bracket the expected force on the beampipe. In the calculation, we assume conservatively that the acoustic field is isotropic. We present the results in Figure 15 for the case of the field measured in the Virgo Central building and the Sos Ennatos tunnel. The expected value of the noise in ET tunnels should lie somewhere in between. The force per unit length amplitude is roughly constant as a function of frequency, which is a result of the falling shape of the spectrum, and the increasing transfer function. The typical value of the force per unit length spectral amplitude one can assume for further calculations is $10^{-4}\mathrm{N\,m^{-1}\,Hz^{-1/2}}$.

9.4 Maximum allowed vibration noise (M. Andres-Carcasona and M. Martinez)

From the information stated in Sec. 2.3, an upper limit on the maximum effective displacement of the baffles can be placed. This movement will inherently depend on the vibration of the ground, the transfer factor between the ground and the baffles, and its phase wrapping. Since both the diffraction and backscattering noises depend linearly on the effective displacement (see Ref. [3]), the upper limit can be placed as the quotient between the safety margin (defined as one order of magnitude below the expected sensitivity) and the projected scattered light noise without the displacement term. The results for the high-frequency and low-frequency interferometers are displayed in Fig. 16. In the case of ET-LF at very low frequencies, the difference between the 1/10 sensitivity curve and the level of scattering noise predicted is very large (spanning many orders of magnitude) leading to very large upper limits on the effective baffle vibration. The use of this limit shall be made with care, applying the phase-wrapping of the actual displacement noise before comparing to it. In particular, at low frequencies the requirement of not exceeding a level of effective displacement will be always satisfied due to the phase-wrapping.

A first modal analysis of the baffle vibration was performed in simulated data for which the baffle is excited with vibrations in the z-direction with amplitude in the range between $0.1\mu m$ and $100\mu m$ in the full frequency range up to 160 Hz (well beyond the range of the existing seismic data). As a result, the mechanical transfer factors between the tube section supporting the baffle and the baffle itself were computed. In the region covered by the existing seismic data (below about 50 Hz), the transfer factor is equal to one. This allows translating the upper limits above on the baffle effective displacement into upper limits on the effective displacement of the tube supports, with the caveats mentioned above that the obtained upper limits might go beyond the realities of the mechanical tolerances and the actual displacements at low frequencies.

Work is in progress to overlay on Figure 16 the effect of baffle/tube vibrations at given fixed amplitudes and frequencies, with the aim to illustrate the actual tolerances and to emphasize the importance of applying the phase-wrapping of the actual displacement noise before comparing with the quoted upper limits on the effective displacement.

9.5 Notes on baffle serration

Here we reproduce the discussion in [3] on the serration of baffles to reduce the induced diffraction noise.

The finite inner aperture produces in each baffle a diffraction pattern that adds up coherently when the baffle has smooth edges. As stated in Ref. [18], the noise generated by the clear aperture of smooth baffles in a centered mirrors cavity can be expressed as

$$\tilde{h}_{\mathrm{smooth}}(f) = \frac{\kappa\lambda X(f)}{\sqrt{2}LR}\sqrt{N_B}\ , \tag{22}$$

where the contributions from N_B baffles are added with no interference, and κ is a parameter extracted from a fit to the tail of the mirror's BRDF using the functional form $\mathrm{BRDF} = \kappa\theta^{-2}$ for $\theta \in [\theta_{\mathrm{min}}, \theta_{\mathrm{max}}]$. The values obtained for κ are $\kappa = 1.32 \times 10^{-7}$ str^{-1} for ET-HF and $\kappa = 1.58 \times 10^{-7}$ str^{-1} for ET-LF.

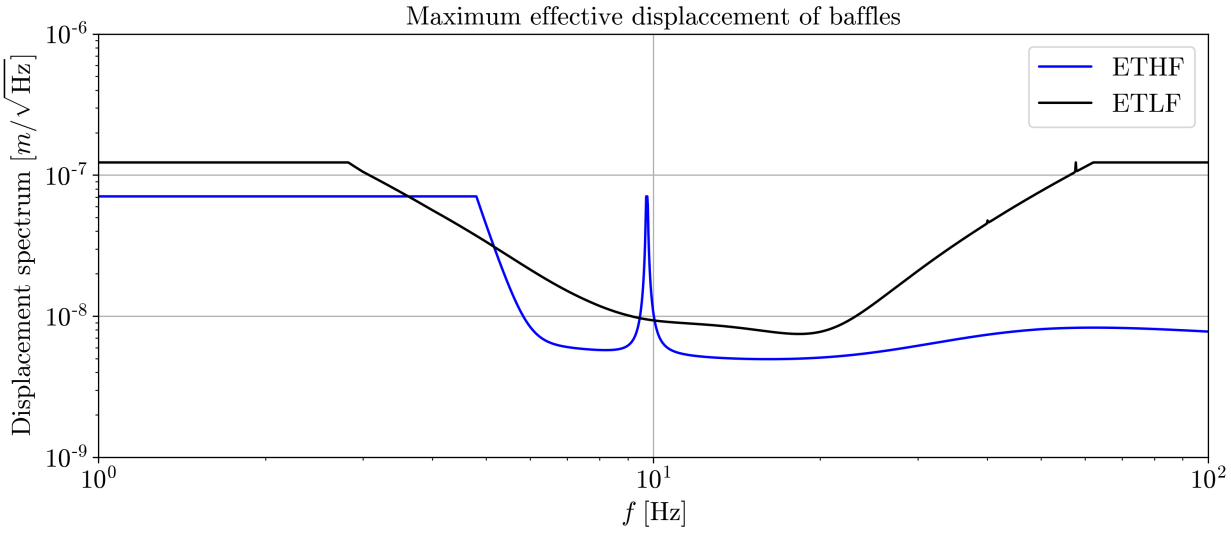

Figure 16: Maximum allowed baffle effective displacement (see body of the text).

As already pointed out, the solution adopted by LIGO and Virgo to mitigate the diffraction noise is to break the coherence in the diffraction pattern by adding a particular triangular serration to the inner edge of the baffles. The peak to valley serration height, denoted by ΔH, must be large when compared to the width of a Fresnel zone [18],

$$\mathcal{W}(z) = \frac{\lambda}{2LR} z(L-z) \ . \tag{23}$$

The maximum Fresnel zone is found at $z = L/2$ and equals $\mathcal{W}_{\rm max} = \frac{\lambda L}{8R}$ which translates into values of 2.66 mm and 3.88 mm for ET-HF and ET-LF, respectively. A peak to valley serration of 1 cm is chosen to ensure that $\Delta H/\mathcal{W} \gg 1$. In order to completely break the coherence this peak to valley height should be randomized by an amount $\gtrsim 2\mathcal{W}$. This translates into a final peak to valley height of $\Delta H = \overline{\Delta H} + \text{Uniform}(-\mathcal{W}, \mathcal{W})$ where the mean height, $\overline{\Delta H}$, is kept as 1 cm and $\mathcal{W} = 4$ mm is chosen to fulfill the requirements for the most restrictive case, corresponding to the baffle placed at the middle of the vacuum tube in the ET-LF configuration. Finally, this serration criteria imposes a lower bound on the baffle length safety margin, dH, as the valleys of the serration could allow photons to reach the tube if the condition

$$dH \geq \frac{\overline{\Delta H} + \mathcal{W}}{\cos(\theta)} \tag{24}$$

is not fulfilled. Altogether, this results into setting the value $dH = 2.44$ cm in Table 18.

The level of diffraction noise in the case of serrated baffles, as defined above, takes the form [18]

$$\tilde{h}_{\rm random}(f) = \frac{\kappa\lambda X(f)\sqrt{N_B}}{LR} \left[\frac{\lambda L}{8\pi R\overline{\Delta H}}\right] \left[\frac{\sqrt{\lambda L/4}}{2\pi R}\right]^{1/2} \ . \tag{25}$$

To account for the radiation pressure on the mirrors, the diffraction noise must be modified by

$$\tilde{h}_{\rm diff}(f) = \tilde{h}_{\rm smooth|random}(f) \sqrt{1 + \left(\frac{8\Gamma P_{circ}}{cM\pi f^2}\right)^2 \frac{1}{\lambda^2}}, \tag{26}$$

where $\tilde{h}_{\rm smooth|random}$ denotes the diffraction noise in Eq. (20) or Eq. (23), Γ represents the gain of the cavity formed by the FP input mirror and the signal recycling mirror [21], and M is the mass of the mirror. The value

for Γ is estimated as in Ref. [21]

$$\Gamma = \frac{1 - r_i r_s}{1 - r_i r_s - r_i + r_s} \ , \tag{27}$$

with r_i and r_s being the amplitude reflectivity of the input mirror and the signal recycling mirror, respectively. In this study we adopt the value $\Gamma = 15.7$.

Table 18 collects relevant baffle parameters.

Baffle parameters				
Variable	ET-HF	ET-LF	Units	Description
A_b	0.84	0.84	[m]	Baffle inner aperture ($R = 0.5$ m)
A_b	1.04	-	[m]	Baffle inner aperture ($R = 0.6$ m)
H	0.14	0.14	[m]	Baffle length
dH	0.0244	0.0244	[m]	Baffle overlapping factor
ϕ	55	55	[deg]	Inclination angle of the baffles
$\frac{\mathrm{d}P}{\mathrm{d}\Omega_{bs}}$	10^{-4}	10^{-4}	[sr^{-1}]	BRDF of the baffles

Table 18: Parameters of the baffles inside the ET vacuum tube.

9.6 Requirements on underground welding. (M.Y. Barel)

This section applies to both configurations

Underground welding concerns two different categories: working safely and keeping the beampipes uncontaminated. The requirements stated here can lead to additional infrastructure requirements and work protocols. But as these are secondary, they are not noted further here.

The main issue with welding is the health implications of the welding fumes, the safe storage of gasses and the use of high currents and voltages. Welding in the tunnel is considered welding in a confined space.

Guidance for National Labour Inspectors on addressing health risks from Welding Fume [43] is a resource from the European Commission, and can be found at circabc.europa.eu. It states that different types of welding processes have different weld fume mixtures. It explains the effects of those fumes, and how to take action to minimize risks.

For ET it is relevant to note that there are 3 documents obligating the employer to take action. (legal framework 1.5) Directive 89/391/EEC contains measures to promote the improvement of the safety and health of workers at work.[8] Directive 98/24/EC of the Council concerning the protection of the health and safety of workers from the risks related to chemical agents [9] and, Directive 2004/37/EC of the European Parliament and of the Council on the protection of workers from the risks related to exposure to carcinogens or mutagens at work (amended by Directive (EU) 2017/2398[15].

Mainly summarizing: These 3 documents above obligate the employer to reduce exposure as much as possible, even if it is below the occupational exposure limit (OEL).

It is recommended to apply a hierarchy of control measures. The directive ranks the following measures in order of preference (1 is first applied, than is 2.. ect):

1. Clean welding techniques are preferred.
2. If welding can be done automatically, this is preferred.
3. If welding can be done in a well-ventilated area with enough space to work around, this is preferred over working in close proximity to the tunnel wall.
4. Ventilation will be essential for safe welding in the tunnel, with local exhaust ventilation being better than general ventilation. Both will be necessary in the tunnel.

5. The number of workers who can be exposed should be kept to a minimum, and workers should be instructed on safe welding in the tunnel, including the proper use of equipment, reducing health and safety risks, and knowledge of tunnel facilities such as fire extinguishing equipment.
6. If all these measures prove insufficient to achieve an acceptable level of exposure, the use of respiratory protective equipment may be required. This could also be made available within the framework of the obligation to reduce occupational exposure, but not be made mandatory if OEL is acceptable.

Remarking point 1: In the case of welding RVS, chrome VI can become airborne and additional safety measures might need to be taken. Max limited exposure is 1 microgram / m^3 [NL] [49].

Remarking to point 4: calculations on ventilation can be executed using:
https://www.5xbeter.nl/site/nl/themas/lasrook
An early indication using this tool gives: A 800 m^3 or a 5-time swap out of the confined space volume is required. Here the heavier ventilation requirement is applied depending on the confined space volume. This needs to be assessed again knowing the type of welding, people involved and exposure time.

Remarking point 6: The OEL is stated to be a maximum of 1 mg/m^3 of occupational exposure to welding fumes per person per day [NL]. This varies per EU country, and there are ongoing developments on stating one OEL for EU. [5]

In general we can conclude on one requirement covering a multitude of health and safety aspects:

Welding in the tunnels				
Requ. number	Name	Value	Units	Description
Req.1	Risk assessment Welding		-	A full risk assessment of the process is required. A HAZOP, a hazard and Operability study, and a FMEA, a failure modes and effect analysis. These are subject to local rules and regulations.

Table 19: Requirements on welding in the tunnels.

10 Acronyms and abbreviations

Acronym	Meaning
BRDF	Bidirectional Reflectance Distribution Function
DOF	Degrees Of Freedom
ET-HF	Einstein Telescope-High Frequency
ET-LF	Einstein Telescope-Low Frequency
FP	Fabry-Perot
FTIR	ourier Transform Infra Red
NEG	Non Evaporable Getter
NVR	Non-Volatile residue
OEL	Occupational Exposure Limit
PSD	Power Spectral Density
RVS	????
TDR	Technical Design Report
TM	Test Mass
UHV	Ultra High Vacuum
XPS	X-ray Photoelectron Spectroscopy

Table 20: Acronyms and abbreviations

References

[1] Allegato 1 - Log di temperatura, conducibilita, gamma ray, resistivita elettrica e caliper. Technical report, I.N.F.N, 14-06-2021. 30

[2] Aharoni Amikam. *Introduction to the theory of ferromagnetism*. Oxford science publications, 1996. 23

[3] M. Andrés-Carcasona, A. Macquet, M. Martínez, Ll. M. Mir, and H. Yamamoto. Study of scattered light in the main arms of the Einstein Telescope gravitational wave detector. *Phys. Rev. D*, 108(10):102001, 2023. 4, 6, 7, 33

[4] M. Angelucci et al. Status of the ET Tower Vacuum, ET-LF Cryostat and ET-LF Payload Cooling Design. Technical Report ET-0235C-22, ET, 2022. 5

[5] Sjögren B, Albin M., Broberg K., Gustavsson P., Tinnerberg H., and Johanson G. An occupational exposure limit for welding fumes is urgently needed. *Scand J Work Environ Health*, 2022 Jan 1; 48(1): 1 - 3, 2022. 36

[6] V. Brisson and J.Y. Vinet. Summary of scattered light noise calculations and baffle design in the long cavities. Technical Report VIR-NOT-LAL-1390-123, VIRGO, 1998. 6

[7] C. Charvet. Procédures d'analyses du laboratoire de chimie - analyse irtf test properté. *EDMS*, 2721632, 2022. 25, 26

[8] The council of the European communities. Directive 89/391/eec, 1989. Official Journal of the European Communities No L. 183/1. 35

[9] The council of the European Union. Directive 98/24/ec, 1998. Official Journal of the European Communities, L. 131/11. 35

[10] C. Torrie D. Coyne. Ftir testing to qualify parts for ligo uhv service. *LIGO E0900480*, 2017. 25

[11] J.-L. Dorier and N. Hilleret. Description of a dust particle detection system and measurements of particulate contamination from shock, gate valve, and ion pump under ultrahigh vacuum conditions. *Review of Scientific Instruments*, 69(11):3818–3827, 1998. 16, 17

[12] S Lederer et al. Particle generation of capacitorr pumps, 2017. Proceedings of IPAC2017, Copenhagen, Denmark. 16

[13] ET science team. Einstein gravitational wave telescope conceptual design study. Technical Report ET-0106C-10, ET, 2011. 4

[14] ET steering committee. ET design report update 2020. Technical Report ET-0007B-20, ET, 2020. 2, 4, 5

[15] The european parliament and the council of the european union. Directive 2004/37/ec, 2004. Official Journal of the European Union L. 229/23. 35

[16] Eric Fest. Stray light analysis and control, 2013. 10, 12

[17] E. Flanagan and K. Thorne. Noise Due to Backscatter Off Baffles, the Nearby Wall, and Objects at the Fare End of the Beam Tube; and Recommended Actions. Technical Report LIGO-T940063-00-R, LIGO, 1994. 6

[18] E. Flanagan and K. Thorne. Light Scattering and Baffle Configuration for LIGO. Technical Report LIGO-T950101-00, LIGO, 1995. 6, 33, 34

[19] E. Flanagan and K. Thorne. Scattered-Light Noise for LIGO. Technical Report LIGO-T950033-00, LIGO, 1995. 5, 6

[20] International Organization for Standardization. ISO 14644-1:1999(E): Cleanrooms and associated controlled environments - Part 1: Classification of air cleanliness. 13

[21] P. Fritschel and H. Yamamoto. Scattered light noise due to the ETM coating ripple. Technical Report LIGO-T1300354, LIGO, 2013. 34, 35

[22] Implenia Oesterreich GmbH. Scope of work for the Civil Engineering Scan for Einstein Telescoop. Technical report, Implenia Österreich GmbH - Tunneling and Civil Engineering, 2019. 30

[23] Aniello Grado, Emanuele Tofani, Marco Angelucci, Roberto Cimino, Julien Gargiulo, Fedor Getman, Andrea Liedl, Luca Limatola, Vito Mennella, Antonio Pasqualetti, Fulvio Ricci, Daniel Sentenac, and Luisa Spallino. Ultra high vacuum beam pipe of the Einstein Telescope project: Challenges and perspectives. *Journal of Vacuum Science Technology B: Microelectronics and Nanometer Structures*, 41(2):024201, March 2023. 21

[24] S. Gerard Jennings, Ronald G. Pinnick, and Harry J. Auvermann. Effects of particulate complex refractive index and particle size distribution variations on atmospheric extinction and absorption for visible through middle ir wavelengths. *Applied optics*, 17 24:3922–9, 1978. 11

[25] KNMI. Gevoelstemperatuur bij warm weer, consulted september 2023. https://www.knmi.nl/kennis-en-datacentrum/uitleg/gevoelstemperatuur-bij-warm-weer. 29

[26] Lifshits E. Landau L. On the theory of the dispersion of magnetic permeability in ferromagnetic bodies. *Phys. Zeitsch. der Sow.*, 8, 1935. 23

[27] LASA. *Corso avanzato di tecnologia del vuoto*. 2019. 25

[28] Mark G Lawrence. The relationship between relative humidity and the dewpoint temperature in moist air: A simple conversion and applications. *Bulletin of the American Meteorological Society*, 86(2):225 – 234, 2005. 30

[29] Angui Li, Risto Kosonen, Arsen Melikov, Bin Yang, Thomas Olofsson, BjÃ¸rn SÃ¸rensen, Linhua Zhang, Ping Cui, and Ou. Han. Ventilation and environmental control of underground spaces: a short review. *E3S WEb of Conference 111:01039*, 2019. 30

[30] Lutz Lilje. Controlling particulates and dust in vacuum systems. Proceedings of the 2017 CERN-Accelerator-School course on Vacuum for Particle Accelerators, Glumslov, (Sweden). 13

[31] M. Martinez M. Andrés-Carcasona, A. Macquet. Progress on stray light noise calculations in the et main arms. ET TDS: ET-0212A-22, 2022. 10

[32] M. Himmerlich M. Taborelli. Standard operating procedure codification of surface cleanliness levels. *EDMS*, 347564 v.8, 2022. 25

[33] Beton Lexicon Aeneas Media. Tempertuurgradiënt, consulted September 2023. https://www.betonlexicon.nl/T/Temperatuurgradiënt. 30

[34] Effendi N., Darwinto T., Agus H.I., and Parikin. 24-chromium ferritic steel magnetic properties. *JusamI*, 395/D, 2012. 24

[35] D.J. Naus. The effect of elevated temperature on concrete materials and structures - a literature review. *Division of Engineering Technology, office of nuclear regulatory research*, 2005. 30

[36] Voci C. Nigro M. *Problemi di FISICA GENERALE.* EDIZIONI LIBRERIA CORTINA PADOVA 1990, 1986. 23

[37] A. Pasqualetti. personal communication, 1 May 2022. 19

[38] T. Porcelli, E. Maccallini, P. Manini, M. Mura, and M. F. Urbano. Experimental methods for the assessment of neg pumps working in dust-sensitive environments, 2018. 16

[39] Contributers: Scott Prahl, Zachary Moon, Yvan Nollet, and Jeffrey Becca. Mie-python package: https://pypi.org/project/miepython/. 11

[40] C. Scarcia. Sectorisation, pumping system, commissioning and operation of et beampipes. https://indico.cern.ch/event/1208957/contributions/5089909/", 2023. 16

[41] S.E. Whitcomb. Optical pathlength fluctuations in an interferometer due to residual gas. Technical report, California Institute of Technology, 1984. 19

[42] Eric Shettle and Robert W. Fenn. Models for the aerosols of the lower atmosphere and the effects of humidity variations on their optical properties. *Environ. Res.*, page 94, 09 1979. 11

[43] Senior Labour Inspectorss Committee (SLIC). Guidance for national labour inspectors on addressing health risks from welding fume, 2018. European Commission, https://circabc.europa.eu/ui/group/fea534f4-2590-4490-bca6-504782b47c79/library/b13cee56-02e8-4b86-9b39-f4c61af8c98c (June 2023). 35

[44] Paul R. Spyak and William L. Wolfe. Scatter from particulate-contaminated mirrors. part 2: theory and experiment for dust and λ=0.6328 μm. *Optical Engineering*, 31(8):1757 – 1763, 1992. 10

[45] ET steering committee Editorial Team. Design Report Update 2020 for the Einstein Telescope. ET-0007B-20, 2020. 23

[46] T. Zhang and S. Danilishin for ISB. Conceptual Design and Noise Budget of Einstein Telescope (ET sensitivity curve update). Technical Report ET-0007B-23, ET, 2023. 7

[47] R. Takahashi, Y. Saito, M. Fukushima, M. Ando, K. Arai, D. Tatsumi, G. Heinzel, S. Kawamura, T. Yamazaki, and S. Moriwaki. Direct measurement of residual gas effect on the sensitivity in tama300. *Journal of Vacuum Science & Technology A*, 20(4):1237–1241, 2002. 19

[48] K. Thorne. Light Scattering and Proposed Baffle Configuration for the LIGO. Technical Report LIGO-T890017-00, LIGO, 1989. 6

[49] Ministerie van Sociale Zaken en Werkgelegenheid. Wat zegt de wet over chrome-6?, consulted may 2023. https://www.arboportaal.nl/onderwerpen/chroom-6/wat-zegt-de-wet-over-chroom-6. 36

[50] Ministerie van Sociale Zaken en Werkgelegenheid. Wanneer is het te warm om te werken?, consulted september 2023. https://www.arboportaal.nl/onderwerpen/warmte/vraag-en-antwoord/wat-is-te-warm. 28

[51] Jean-Yves Vinet, Violette Brisson, and Stefano Braccini. Scattered light noise in gravitational wave interferometric detectors: Coherent effects. *Phys. Rev. D*, 54:1276–1286, 07 1996. 6

[52] Jean-Yves Vinet, Violette Brisson, Stefano Braccini, Isidoro Ferrante, Laurent Pinard, Fran çois Bondu, and Eric Tournié. Scattered light noise in gravitational wave interferometric detectors: A statistical approach. *Phys. Rev. D*, 56:6085–6095, Nov 1997. 10

[53] K Agricola W Whyte and M Derks. Airborne particle deposition in cleanrooms: Relationship between deposition rate and airborne concentration. *Clean Air and Containment Review*, 25, 2016. 14

[54] Wen Yueming, Leng Jiawei, Shen Xiaobing, Han Gang, Sun Lijun, and Yu Fei. environmental and health effects of ventilation in subway stations: A literature review. *International journal of environmental research and public health*, 2020. 30

[55] M. E. Zucker and Stanley E. Whitcomb. Measurement of Optical Path Fluctuations due to Residual Gas in the LIGO 40 Meter Interferometer. In Robert T. Jantzen, G. Mac Keiser, and Remo Ruffini, editors, *Proceedings of the Seventh Marcel Grossman Meeting on recent developments in theoretical and experimental general relativity, gravitation, and relativistic field theories*, page 1434, January 1996. 19